

Winds at the Mars 2020 landing site.

Part 1: Near-surface wind patterns at Jezero crater

D. Viúdez-Moreiras^{1,*}, M. Lemmon², C.E. Newman³, S. Guzewich⁴, M. Mischna⁵, J. Gómez-Elvira⁶, A. Sánchez-Lavega⁷, K. Herkenhoff⁸, M. de la Torre⁵, J.A. Rodríguez-Manfredi¹, R.D. Lorenz⁹, S. Navarro¹, J. Pla-García¹, R. Hueso⁷, M. Richardson³, M. Smith⁴, V. Apéstigue⁶, D. Toledo⁶, J. Bell¹⁰

¹Centro de Astrobiología (CSIC-INTA) & National Institute for Aerospace Technology (INTA), Torrejón de Ardoz, Madrid, Spain (viudezmd@inta.es)

²Space Science Institute, College Station, TX 77843 USA.

³Aeolis Research, Chandler, AZ, USA.

⁴NASA Goddard Spaceflight Center, Greenbelt, MD, USA.

⁵Jet Propulsion Laboratory, California Institute of Technology, 4800 Oak Grove Drive, Pasadena, CA 91109, USA.

⁶National Institute for Aerospace Technology (INTA), Torrejón de Ardoz, Madrid, Spain

⁷Universidad del País Vasco (UPV/EHU), Bilbao, Spain

⁸USGS Astrogeology Science Center, Flagstaff, AZ 86001, USA.

⁹Johns Hopkins Applied Physics Lab, Laurel, MD, USA.

¹⁰School of Earth and Space Exploration, Arizona State University, Tempe, AZ 85281, USA.

ABSTRACT

This is the first part of a two-part paper. NASA's Mars 2020 Perseverance rover measured winds on the Jezero crater floor close to the delta of an ancient river. A mostly repeatable diurnal cycle was observed and presented two regimes: (i) a convective regime, from dawn to sunset, with average easterly to southeasterly winds, during which maximum wind speeds were measured, and (ii) a nighttime regime with westerly-northwesterly winds followed by a relatively calm period with highly variable wind directions as a function of sol and time of night. The timing and magnitude of the observed regimes is consistent with primary control by regional and local slope flows. Data suggest that the surface circulation at Jezero region is highly unaffected by large-scale circulation except during particular periods in the diurnal cycle or, generally, during dust storms. Consequently, the seasonal variability in northern spring and summer seasons was weak. However, sol-to-sol and seasonal variability were measured, most of it during certain nighttime periods. Traveling waves consistent with baroclinic instability were clearly observed in surface winds at $L_s \sim 75^\circ$. The early MY36/2022 regional dust storm at $L_s \sim 153^\circ$ disturbed the wind patterns with changes suggesting enhanced tidal flows. After sunset, the dust storm also produced detectable gravity wave activity, increasing the mixing in the nighttime planetary boundary layer during storm conditions.

PLAIN LANGUAGE SUMMARY

This is the first part of a two-part paper. NASA's Mars 2020 Perseverance rover landed close to the western rim of Jezero crater (18.44°N, 77.45°E) on Feb 18, 2021. The wind data acquired by the rover measured a mostly repeatable diurnal cycle with two regimes: (i) a convective regime, from dawn to sunset, with average easterly to southeasterly winds, in which maximum wind speeds were measured, and (ii) a nighttime regime with westerly-northwesterly winds followed by a relatively calm period with highly variable wind directions as a function of sol and time of night. The timing and magnitude of the observed regimes is consistent with primary control by regional and local slope flows, as has been observed to varying degrees at other landing sites on Mars. Data suggest that the surface circulation at Jezero is highly unaffected by large-scale circulation, except during particular periods. An early regional dust storm prior to fall equinox also disturbed wind patterns, with changes suggesting the strengthening of flows linked to

53 large-scale atmospheric oscillations called tides. The latter are primarily driven by the daily pattern of solar
54 heating around Mars and its interaction with topography.

55
56
57

58

59 **KEY POINTS:**

60 1. A mostly repeatable diurnal cycle is consistent with primary control by regional and local
61 slope flows.

62 2. Great sub-diurnal and sol-to-sol variability was observed during the calm period at night.

63 3. Atmospheric and gravity waves were observed, along with the probable effect of enhanced
64 tidal flows.

65

66 **1. INTRODUCTION**

67 NASA's Mars 2020 Perseverance rover successfully landed close to the western rim of Jezero crater
68 (18.44°N, 77.45°E) on February 18, 2021 (areocentric solar longitude, $L_s \sim 5^\circ$). The rover is seeking signs of
69 potential ancient life on Mars and preparing, for the first time, a set of samples for possible return to Earth
70 (Farley et al., 2020). Among the mission objectives, Mars 2020 should enable future Mars exploration
71 focused on manned missions, with a characterization of the atmospheric environment. To fulfill this
72 requirement, the Mars Environmental Dynamics Analyzer (MEDA) instrument (Rodríguez-Manfredi et al.,
73 2021) on board Perseverance rover includes a wind sensor that combines with other meteorological
74 measurements to allow the characterization of the atmospheric environment of Jezero crater and obtain
75 insight into the processes that drive the Martian atmosphere.

76 Near-surface winds are a key mechanism for the exchange of heat, mass and momentum between the
77 surface and the atmosphere. On Mars, suspended dust in the atmosphere drives weather and climate.
78 Therefore, comprehensive knowledge of the surface wind patterns is desirable to fully understand the
79 weather and climate of the planet, as well as how dust storms originate and develop. To date, however, few
80 missions have measured the surface winds on Mars, and their measurement has been complex and
81 sometimes constrained by instrumentation issues. The first measurements of the Martian winds were taken
82 by the Viking Landers (VL) in the 1970s at 22.5°N 48°W (VL-1) and at 48°N 134°E (VL-2). Those
83 missions observed light winds of a few meters per second with a marked rotation in the diurnal cycle. They
84 also reported dramatic changes as a function of season and in the presence of dust events, which were
85 attributed to variable regional slope flows, diurnally varying planetary boundary layer (PBL) coupling,
86 large-scale circulation, thermal tides and baroclinic waves (Hess et al., 1977; Ryan et al., 1978; Barnes et
87 al., 1980; Murphy et al., 1990).

88 Twenty years later, the Mars Pathfinder mission again measured Martian surface winds. The Pathfinder
89 lander acquired sparse wind data during several sols and enabled the first direct measurements of near-
90 surface wind profiles on Mars, including a determination of aerodynamic roughness length and wind
91 friction speeds (Sullivan et al., 2000). Later, the Phoenix lander measured winds (Holstein et al., 2010) in
92 the polar region (68.2°N 125.8°W) and at various heights during ~150 mission sols, showing highly
93 variable diurnal conditions due to the daytime convective turbulence and reporting wind patterns possibly

94 driven by thermal tides and weather systems. The Mars Science Laboratory (MSL) measured surface winds
95 at Gale crater, but the retrieval presented problems due to damage to the wind sensor during MSL's
96 landing. A comprehensive diurnal and seasonal surface wind characterization was presented covering the
97 two Mars years over which the wind sensor operated, in the northwest crater floor and on the northwestern
98 slopes of Aeolis Mons. Wind data showed that the patterns at Gale crater are driven mostly by local slope
99 winds on Aeolis Mons, in accordance with mesoscale model predictions (Tyler et al., 2013; Raftkin et al.,
100 2016; Pla-García et al., 2016; Newman et al., 2017; Viúdez-Moreiras et al., 2019a; 2019b). To date, these
101 wind patterns are the most complex ever seen on Mars, due to strong constructive and destructive
102 interactions between different scales variably affecting the near-surface atmosphere in the crater. Wind-
103 driven erosion signatures and sand transport have also been repeatedly observed by the mission (e.g.,
104 Sullivan & Kok; 2017; Schieber et al., 2021; Vasavada, 2022 and references therein). Local winds in Gale
105 crater have been proposed to drive the abundance of methane detected by MSL near the surface, and could
106 even induce advective flows in the regolith (e.g. Webster et al., 2018; Etiope & Oehler; 2019; Viúdez-
107 Moreiras et al., 2020a; 2021).

108 InSight landed in Elysium Planitia (~4.5°N 136°E) right after the decay of the MY34/2018 Global Dust
109 Storm (GDS) and before the onset of the MY34/2019 Large Dust Storm (LDS) (e.g. Montabone et al.,
110 2020). Before and after the storm began, the observed wind patterns resulted from the interaction between
111 regional and local slope flows induced by topography, together producing a diurnal perturbation
112 superimposed on a mean flow, dominated by the Hadley cell but with modifications due to channeling
113 effects from the regional topography (Banfield et al., 2020; Viúdez-Moreiras et al., 2020b). Pressure tides
114 were strongly affected by the LDS and produced a dramatic change in the wind patterns that was attributed
115 to enhanced tidal flows. InSight's surface wind measurements have also been crucial for aeolian studies.
116 Aeolian changes at InSight's landing site in Elysium Planitia were infrequent and probably primarily driven
117 by high wind speeds inside convective vortices (Charalambous et al., 2021). The effect of ambient wind
118 speeds on convective vortex encounters was also observed (Spiga et al., 2021) and wind measurements
119 inside vortices were reported, complementing those observed by MSL (Banfield et al., 2020; Spiga et al.,
120 2021; Kahanpää & Viúdez-Moreiras, 2021).

121 Mars 2020 has detected a rich dynamic atmosphere and aeolian environment in Jezero crater with dust
122 lifting mainly produced by the passage of convective vortices and convection cells (Newman et al., 2022;

123 Bell et al., under review; Rodríguez-Manfredi et al., under review). Measurements obtained during the first
124 few sols of the mission suggested that wind patterns are mainly controlled by regional and local slope
125 flows. Perseverance also characterized an early MY36/2022 regional dust storm in January 2022, which
126 produced several dust-lifting events (Lemmon et al., this issue). The strong aeolian activity observed at
127 Jezero has produced side effects on the instrumentation. The Mars 2020 wind sensor has been
128 systematically damaged throughout the mission, although efforts are being made to partially recover most
129 of the functionality. Furthermore, Mars 2020 has deployed, for the first time, an unmanned aerial vehicle on
130 another planet, the Ingenuity helicopter (Farley et al., 2020; Balaram et al., 2021), whose safety is strongly
131 dependent on atmospheric conditions. Together with the InSight's wind sensor, the Mars 2020 wind sensor
132 is currently operating on the Martian surface.

133 In this two-part paper, we present the winds at the Mars 2020 landing site on the Jezero crater floor. This
134 part focuses on the Mars 2020 MEDA wind measurements, describing the mechanisms that may be
135 involved in the near-surface wind patterns at Jezero and presenting the observed winds throughout the
136 mission from the diurnal to the seasonal scales, including the effects of the MY36/2022 regional dust storm
137 on the near-surface circulation at Jezero. The second part presents the observed wind variability focusing
138 on the sub-diurnal scale. This first part is structured as follows: Section 2 describes the MEDA wind sensor
139 observations and the support that the wind measurements provided for the first Ingenuity flights. Section 3
140 introduces the mechanisms that may affect the near-surface wind patterns at Jezero crater. Section 4 shows
141 the diurnal cycle of winds at Jezero, and Section 5 the sol-to-sol and seasonal cycle for the period covered
142 by the sensor. Section 6 presents the effects of the MY36/2022 regional dust storm. Finally, Section 7
143 presents the conclusions.

144

145 **2. METHODS: THE MARS 2020 MEDA WIND SENSOR AND OBSERVATIONS**

146 **2.1 The Mars 2020 MEDA wind sensor**

147 The Mars 2020 MEDA wind sensor (WS) consists of two booms (WS1 and WS2) angled at 120° to each
148 other and mounted on the Perseverance's Remote Sensing Mast (RSM), as shown in Fig. 1. WS1 points to
149 the direction of the rover movement with a displacement of 6° in azimuth (Rodríguez-Manfredi et al.,
150 2021), with the WS2 rotated 120° clockwise to the WS1. The WS measures winds by thermal anemometry,

151 as in the Viking landers, MSL and InSight WS (Hess et al., 1977; Gómez-Elvira et al., 2012; Banfield et al.,
152 2020), using thin-film resistors patterned on the surface of a silicon chip. Placed at 1.5 m above the ground,
153 each boom has six sensor boards angled differently to the incoming wind direction, in different planes. The
154 six sensor boards included on each boom allow for substantial redundancy in wind retrieval and enable
155 accurate measurement of vertical winds, significantly improving the preceding designs implemented in the
156 MSL and in the InSight wind sensors.

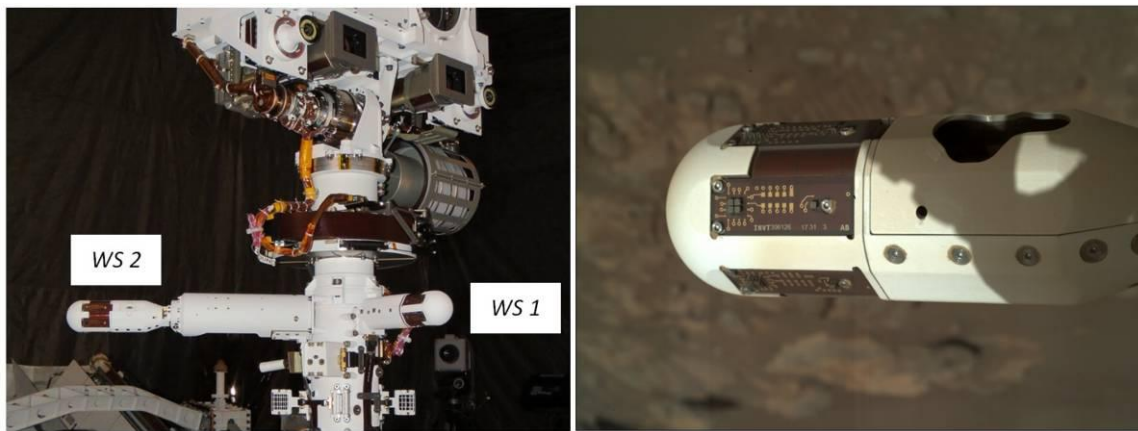
157 As in previous missions, the measured winds can be affected by the rover or platform itself, i.e., the
158 ambient winds can be perturbed by the presence of the rover and thus the measured winds could differ from
159 the ambient winds. The Perseverance rover is mostly similar to the MSL Curiosity rover in terms of both
160 the platform and in the sensor allocation, with the RSM being the main source of perturbation. The position
161 of the booms allows for the selection of the best boom for an incoming wind direction. On MSL, based on
162 thorough CFD modeling and examination of REMS wind measurements after the sensor damage during
163 MSL's landing, accurate wind speeds and directions were retrieved only for winds coming from the front
164 boom hemisphere with incident wind angles between -90° and $+90^\circ$ relative to the boom (Gómez-Elvira et
165 al., 2012; Viúdez-Moreiras et al., 2019a). Perseverance WS2 was designed to minimize the RSM
166 perturbation and other disturbances by using a larger WS2 boom (393 mm versus 170 mm). Allocation and
167 mechanical constraints on the Perseverance rover to be experienced during the cruise stage prevented the
168 inclusion of a fixed WS2, which led to the development of a deployable boom once on the Martian surface.
169 Thus, the sensors are farther from the RSM, allowing wider incident angles to be retrieved, particularly
170 those of the WS2 boom, thus strongly minimizing the uncertainties in the rear hemisphere of the rover.
171 Individual wind speeds and directions were estimated at each boom from all six sensor boards based on a
172 wind tunnel calibration database augmented by CFD modeling, correcting potential disturbances from the
173 RSM and its appendages, and combined according to the incident wind direction.

174 Mars 2020 wind data incorporates a relatively new issue that must be considered. The radioisotope
175 thermoelectric generator (RTG) generates a thermal plume that could perturb the flow towards the sensors
176 if the incoming wind direction comes from the rover's rear hemisphere. This thermal disturbance was not
177 involved in the MSL REMS data, given that only the front pointing wind sensor boom was available to
178 retrieve winds due to damage on the rear boom at MSL's landing. The RTG can provoke disturbances in
179 the wind measurements, mainly in wind speeds. Thus, winds coming from the rear angles close to the RTG

180 were not considered in this study. Fortunately, as in MSL, the rover moves regularly, so the attitude
181 changes accordingly and the winds are sampled from every direction throughout the mission, despite gaps
182 that are present if the rover is placed for long time at the same attitude.

183 MEDA WS can characterize the horizontal component of the wind at the sensor location with a resolution
184 of at least 0.5 ms^{-1} in speed in the $0\text{-}10 \text{ ms}^{-1}$ range, and of 1 ms^{-1} for wind speeds above 10 ms^{-1} up to 40
185 ms^{-1} . The performance decreases for temperatures greater than 223 K , reaching 1.25 ms^{-1} resolution at 293
186 K .

187



188

189

190 **Fig. 1:** (left) MEDA wind sensor booms (WS1 and WS2) on Mars 2020 Perseverance's Remote Sensing
191 Mast (RSM) (right) MEDA WS2 captured on the Martian surface by the SHERLOC WATSON camera,
192 onboard Perseverance, as part of the study performed after the event on sol 313. Credit: NASA/JPL-
193 Caltech.

194

195

196

2.2 The Mars 2020 wind measurements and observations

197 The MEDA instrument performed eventual measurements beginning with sol 1, and starting systematic
198 operations on sol 28 (Fig. 2). The MEDA WS2 was deployed on sol 10 (Feb 28, 2021). Discrepancies in
199 the obtained results on Mars and the malfunction of a sensor board on WS2 delayed the start of WS
200 operations to sol 36. Mars 2020 operational constraints limited the measurements in the first sols, focusing
201 the observations on supporting the Ingenuity helicopter flights, particularly to select the best time of the day
202 to minimize the risks for the first flights. The primary helicopter campaign concluded on sol 75, thus
203 starting nominal wind observations, including additional coverage of morning, night-fall and nighttime
204 since then. MEDA measurements were acquired for even or odd Martian hours, alternatively, from sol to
205 sol, in Martian local mean solar time (LMST). In addition to these background hourly measurements,

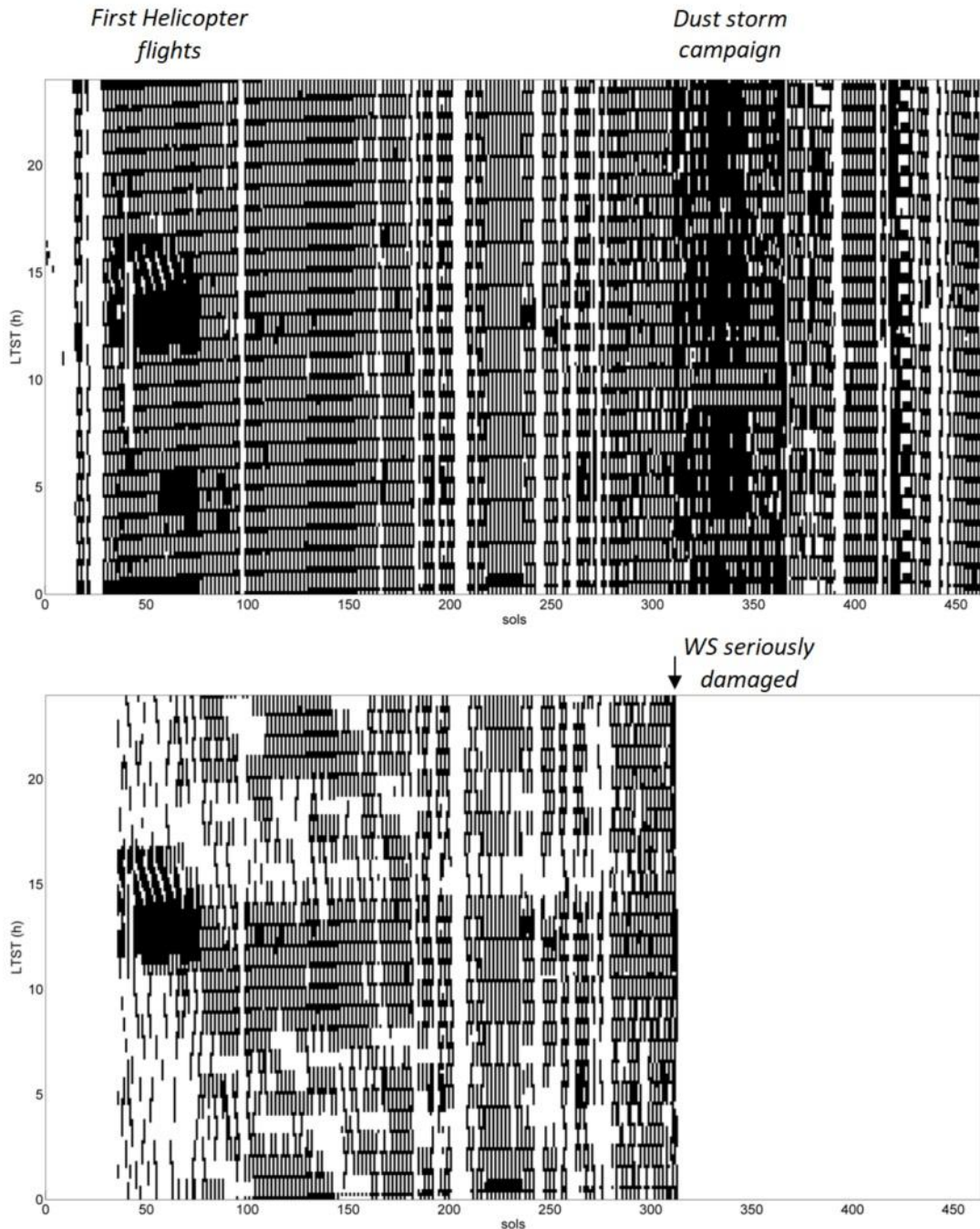
206 extended blocks may be included in each plan considering the operational constraints of the Perseverance
207 rover. A potential issue between the WS and the antenna of the rover meant that the WS had to be turned
208 off during the ultra high frequency (UHF) communication passes of the satellites, thus losing those wind
209 observations.

210 Given the high sub-diurnal, diurnal and intersol variability inherent in winds, this sampling, together with
211 significant gaps due to the satellite passes, prevented proper characterization of certain features in the wind
212 data. Measurement cadence was increased at sol 281 after optimizing wind observations in the Mars 2020
213 tactical plans. The arrival of the MY36/2022 regional dust storm led to the activation of the dust storm
214 campaign on sol 311 (Fig. 2), with continuous observations along several hours, significantly enhancing the
215 wind data over those sols. Observations began at a 2 Hz sampling frequency, lowered to 1 Hz after sol 152,
216 due to the need to extend the observation times while maintaining the operational constraints on data
217 volume.

218 Flying debris is known to damage instrumentation in the severe conditions present on the Martian surface.
219 MSL REMS WS was damaged during MSL's landing, due to flying debris making one of the two sensor
220 booms inoperative. Dust aerosol impacts occurring due to the strong winds observed during the latest
221 operational period of the sensor (around the southern spring equinox while approaching Aeolis Mons) are
222 believed to be the responsible for the final REMS WS sensor failure on MSL after ~1500 sols of the
223 mission (Viúdez-Moreiras et al., 2019a; 2019b). As a result of the MY36/2022 regional dust storm, the
224 convective and aeolian activity at Jezero increased dramatically. A close encounter with a dust devil on sol
225 313 at 13:42 h LTST further damaged WS2 (see the companion paper, part 2). Two sols later (sol 315 at
226 14:24 h LTST), damage was produced on WS1 and the MEDA WS was unavailable to provide wind data,
227 leaving only three operative sensor boards: one on WS2 and two on WS1. The sensor was turned off while
228 an engineering analysis was performed. Detailed images obtained with the Mars 2020 cameras (Fig. 1) on
229 sol 339 suggested damage on the board wires due to the impacts of lifted dust. The sensor was again turned
230 on, on sol 342, although without retrieving wind data products. Further damage on other boards during the
231 regional dust storm was detected, continuing at sol 413 and making the sensor inoperative to retrieve data
232 without major modifications to the pipeline and additional calibration tests in the wind tunnel. It is expected
233 that wind data from sol 342 to 413, and possibly data since sol 413, will be available when the retrieval

234 algorithm for each boom is modified to focus on the non-damaged boards of the sensor, although greater
235 uncertainty in the wind data will be involved in the retrievals.

236



237
238 **Fig. 2:** (top) MEDA instrument observations performed until sol 450, as a function of LTST. The special
239 campaigns to support the first helicopter flights (sol 28-75) and to widely cover the 2022/MY36 regional
240 dust storm (sol 311-364) are highlighted. (bottom) MEDA instrument observations including WS
241 measurements over the same period. The WS measurements started on sol 35 after the commissioning
242 period. The WS was damaged during periods of high convective activity, probably by suspended dust, on
243 sol 313 (WS2) and 315 (WS1).
244

245
246

2.3 Dust devil trajectories as a background wind proxy

247 In the absence of a working wind sensor, surface winds may be inferred, under particular conditions, from
248 other sensors and/or from their interaction with surface. We have attempted to obtain some information on
249 surface winds from dust devil Navcam surveys or movies after the wind sensor damage. Some surveys or
250 movies detected the passage of dust devils (DDs) and, if conditions were appropriate, it was possible to
251 estimate the trajectory of DDs from cameras. Terrestrial field measurements showed that dust devil
252 horizontal speed is in agreement with wind speeds a few tens of meters above the surface, and that their
253 horizontal direction closely matches background wind directions (Stanzel et al 2008; Balme et al., 2012).
254 Therefore, assuming that DDs move with the background winds (e.g., Stanzel et al 2008; Reiss et al.,
255 2014), the background wind direction can be inferred. Buoyancy-driven turbulent activity present in the
256 PBL during the day can deviate local winds from the background wind, producing continuous disturbances
257 (see companion paper, part 2); thus DD trajectories may deviate from the average wind in some cases.

258 Dust lifting events were detected in Navcam surveys or movies. Each comprised $96 \times 19^\circ$ subframed images
259 of 1280×240 pixels. For movies, one aim was used for 21 images over ~ 90 s. For surveys, 5 aims were
260 imaged 3 times, with ~ 4 s between images at one aim. Images were processed following Greeley et al.
261 (2006) by constructing a mean or median frame and subtracting that frame from each image at the same
262 pointing (per-pixel median frames were used for sets of 3). Images were inspected for changing features, all
263 of which were visually confirmed to be lifted dust in motion (excluding obvious illumination artifacts). All
264 reported dust detections were consistent with dust devils except one on sol 472, which had an amorphous,
265 gust-like appearance. For each sequence with dust lifting, wind direction was assessed visually. Transverse
266 (azimuthal) motion was measured, and radial motion was inferred where possible. Uncertainties range from
267 unconstrained radial motion (45°) to well-constrained radial motion (15°); when multiple dust devils were
268 tracked in one sequence, all were used to infer an average wind motion (Stanzel et al 2008).

269

2.4 MEDA wind measurements supported the first flights on Mars

271 The successful landing of Perseverance on Mars brought with it a partner, the technology demonstration
272 helicopter Ingenuity (Farley et al., 2020; Balaram et al., 2021), designed to demonstrate the capability of

273 powered flight in the Martian environment. Given the a priori absence of atmospheric information in Jezero
274 crater, and the need to understand both density and wind conditions in the local environment, a significant
275 modeling effort was pursued, prior to landing, in order to constrain the expected flight environment (e.g.,
276 Mischna et al., 2021). Upon landing, the mission timeline dictated an early demonstration of Ingenuity's
277 capabilities, and it was expected that the first flights would occur prior to full commissioning of the MEDA
278 wind sensor (the air temperature and pressure sensors were commissioned sufficiently early so as to
279 provide useful density information early in the mission).

280 Due to engineering constraints on Ingenuity, flights could initially only occur during late morning and
281 afternoon, to ensure adequate temperatures for helicopter electronics (dictating the start of the window),
282 and a sufficient battery state of charge to support helicopter heating during the subsequent overnight period
283 (dictating the end of the window). Thus, the initial activities sought to assess the wind environment
284 between 10 h and 17 h LMST. Initial assessment of wind speed and direction was performed beginning on
285 sol 38 of the mission using calibrated MEDA wind sensor data, and showed two consistent diurnal trends.
286 First, there was an observed pattern of increasing mean wind speed over the course of the study window,
287 from ~5 m/s at 10 h LMST to peak winds of ~11 m/s by 17 h LMST (see the companion paper, part 2), in
288 agreement with numerical modeling estimates of large-scale wind speed. The Ingenuity helicopter had
289 previously been tested against mean wind speeds of up to 11.2 m/s prior to launch, with satisfactory
290 performance, and so the MEDA mean wind speed measurements were not considered a significant
291 constraint on flight time. Second, wind speed variability, or small-scale turbulent activity, decreased
292 modestly throughout the sol, showing a broader range of wind speeds during the late morning and mid-sol
293 period ($\sigma_v < 4$ m/s), with a narrowing range ($\sigma_v \sim 2$ m/s) after ~15.5 h LMST (see the companion paper, part
294 2). This, too, was consistent with modeling studies, and reflects the growth of larger-scale convective cells
295 at the expense of small-scale, turbulent motions. Wind direction was not considered a significant constraint
296 on Ingenuity operations, but was monitored for later assessment of helicopter performance.

297 Based in large part on this input from the MEDA wind sensor, early Ingenuity flights, starting with the first,
298 historic flight on sol 58, were performed at 12.5 h LMST, this time being seen as a suitable balance
299 between lower mean wind and moderate potential for turbulent motion, thus minimizing atmospheric risks
300 to helicopter activities. Table 1 shows the atmospheric conditions during the first flight of Ingenuity, in
301 which there are wind data available. Fig. 4 shows the trajectories for each flight. Mean wind speed during

302 the flights was 4.6 m/s at 1.5 m (7.3 m/s at 10 m assuming a neutrally stable atmosphere, which probably
 303 overestimates wind speeds), with a mean pressure and temperature of 725 Pa and 238 K, respectively.

304 As the team gained confidence in Ingenuity’s performance, flights later in the sol were performed, as
 305 MEDA continued to return data consistent with the previously observed trends. Following each flight, data
 306 were requested from the MEDA team, spanning the period of flight, for later comparison to flight
 307 performance logs, to identify any possible environmental conditions which might have led to off-nominal
 308 helicopter behavior (though no such conditions were observed).

309

F	Earth Date (UTC)	L_s (deg)	sol	LTST (h)	Flight duration (sec)	P_{srf} (Pa)	$T_{1.5\text{m}}$ (K)	$\rho_{1.5\text{m}}$ (kg/m ³)	$\phi_{1.5\text{m}}$	$\sigma_{\phi_{1.5\text{m}}}$	$v_{1.5\text{m}}$	$\sigma_{v_{1.5\text{m}}}$	max $v_{1.5\text{m}}$	min $v_{1.5\text{m}}$
01	19 April 2021 07:34	33.5	58.5	12.26	40	748.4	235.8	0.0165	142.1	25.5	5.6	1.8	10.0	1.6
02	22 April 2021 09:33	34.9	61.5	12.29	52	748.6	235.9	0.0165	62.8	56.5	4.0	1.9	9.6	0.2
03	25 April 2021 11:31	36.3	64.5	12.29	80	746.5	236.8	0.0164	85.7	64.1	4.4	1.7	11.2	0.5
04	30 April 2021 14:49	38.7	69.5	12.32	117	748.1	235.3	0.0166	113.9	43.8	4.3	1.7	8.4	0.7
06	23 May 2021 05:20	48.8	91.5	12.45	140	751.7	236.0	0.0166	-39.9	79.2	3.3	1.9	8.9	0.4
07	08 June 2021 15:54	56	107.5	12.54	63	754.8	237.3	0.0166	110.2	39.6	4.6	2.4	12.2	0.3
08	22 June 2021 00:27	61.9	120.5	12.57	77	752.6	238.0	0.0165	78.3	20.0	6.4	2.8	19.1	1.0
12	16 August 2021 12:57	86.1	174.6	13.60	170	715.8	245.2	0.0152	109.6	32.8	3.6	1.3	8.4	0.4
14	24 Oct 2021 08:18	117.1	241.5	12.92	23	650.7	242.3	0.0140	64.5	31.6	5.7	2.1	11.9	1.0
16	21 Nov 2021 02:09	130.2	268.5	13.02	108	633.7	240.5	0.0137	42.4	34.0	3.9	1.5	7.9	0.7

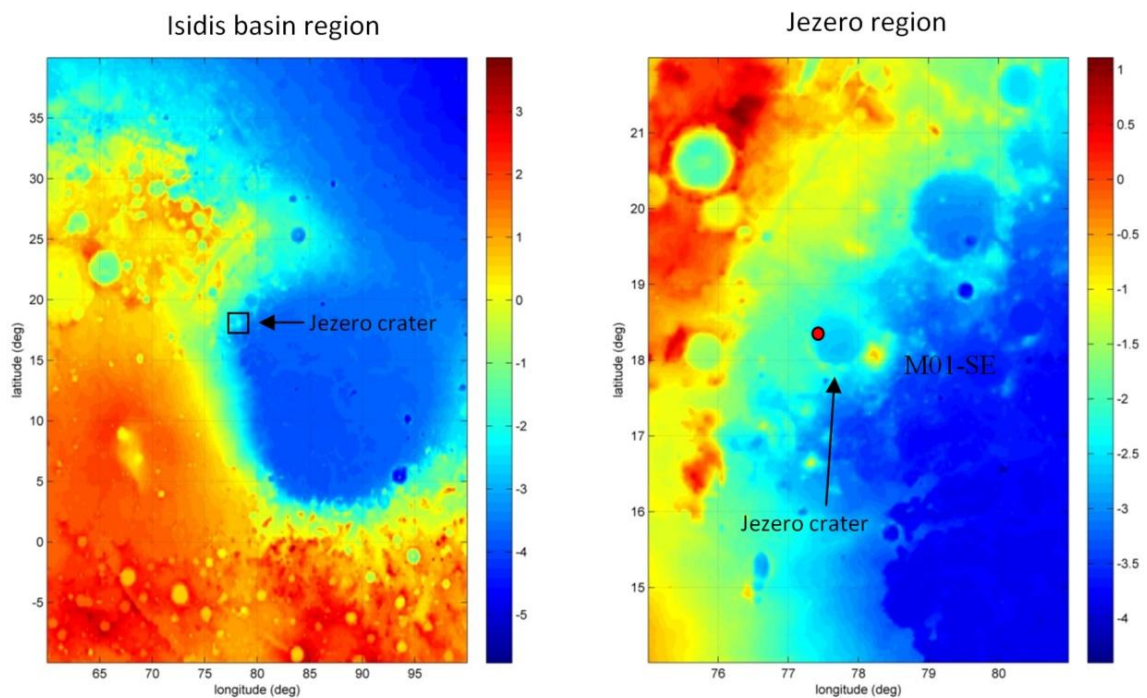
310 **Table 1:** Atmospheric conditions and winds during the Ingenuity helicopter flights with available MEDA
 311 wind data. Pressure (P_{srf}), temperature ($T_{1.5\text{m}}$) and estimated density ($\rho_{1.5\text{m}}$) at 1.5 m are included, as well as
 312 mean and standard deviation of wind direction ($\phi_{1.5\text{m}}$ and $\sigma_{\phi_{1.5\text{m}}}$) and speed ($v_{1.5\text{m}}$ and $\sigma_{v_{1.5\text{m}}}$) as measured by
 313 MEDA. Also, maximum and minimum wind speeds obtained by MEDA during the flights are shown.
 314

315 3. INFLUENCES ON THE JEZERO CRATER CIRCULATION

316 Surface wind patterns in the tropical region of Mars could be the consequence of complex interactions
 317 between slope flows, on regional and local scales, and the large-scale circulation, dominated by Hadley cell
 318 flows, thermal tides and other planetary waves. In addition, other topographic influences, microscale flows,
 319 turbulence and wave activity modify this situation.

320 Jezero is an impact crater of 45 km in diameter and more than 500 m deep from the surroundings, with
321 crater rims elevated ~ 800 m to the W and ~ 1 km to the S above the crater floor (e.g., Schon et al., 2012).
322 Jezero is located on the northwestern slopes of Isidis basin (Fig. 3), a region presenting a steep slope ($\sim 0.7^\circ$
323 downward towards $\sim 120^\circ$ of azimuth, clockwise from the north). This slope suggests strong near-surface
324 regional flows in the area. In fact, the Isidis regional slope in the Jezero region is significantly greater than
325 the $<0.1^\circ$ general slope of other landing sites, e.g., for Viking Lander 1 and InSight, where wind patterns
326 were significantly shaped by regional slope flows (e.g., Hess et al., 1977; Banfield et al., 2020; Viúdez-
327 Moreiras et al., 2020). Thus, it was expected pre-landing that the regional flows on the Isidis basin slopes
328 may shape the surface wind patterns.

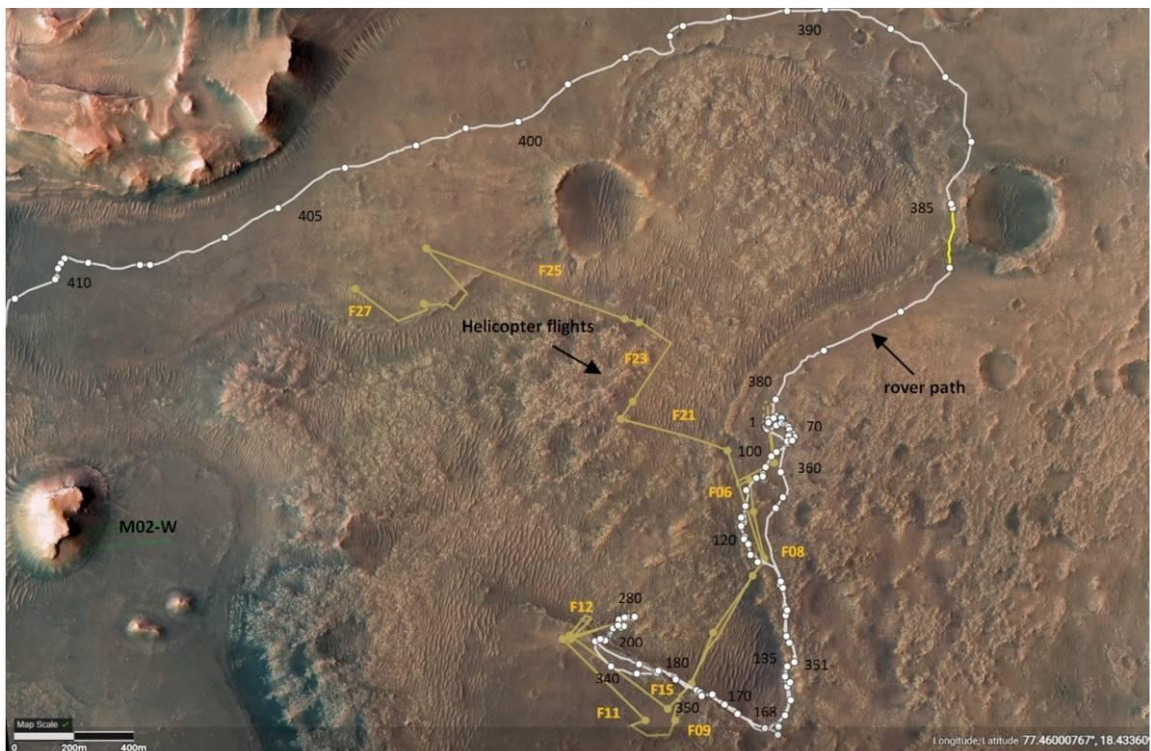
329 Additionally, local dynamics were expected in Jezero crater. To date, the only mission to measure winds in
330 a region with significant topography at the local scale was MSL, which operates inside Gale crater. MSL
331 observed wind patterns shaped by local slope flows related to both the rim of the crater and the mountain in
332 the center of Gale (Newman et al., 2017; Viúdez-Moreiras et al., 2019a). Perseverance's landing site is
333 close to the western-northwestern rims of Jezero crater, where slope flows are expected to develop.
334 However, Jezero crater is smaller and far shallower than Gale crater, and does not contain a central mound,
335 so the potential relevance of local slopes on wind patterns should be addressed by observations and
336 modeling.



337

338 **Fig. 3: (left)** MOLA topography for the Isidis basin region. **(right)** Enlargement for the Jezero crater region. Perseverance's location is highlighted with a red circle close to the northwest crater rim of Jezero crater. Altitude is shown in kilometers both in left and in right panels.
 339
 340
 341

342



343

344 **Fig. 4:** High resolution images of the landing site location close to the western crater rim, taken from Mars
345 Reconnaissance Orbiter (MRO). **(top)** crater rim and Jezero's delta **(bottom)** Enlargement of the
346 southeastern region around the Mars 2020 landing site. The Perseverance rover and the Ingenuity helicopter
347 trajectories as far as sol 410 are highlighted in the bottom panel in white and yellow colors, respectively.
348 Mission sols are included in black and helicopter flights are labeled in yellow.
349

350 Other influence in the observed wind patterns by a mobile platform is the change in location throughout its
351 traverse, that is, surface winds are observed in this case by a rover instead of by a fixed platform. It enables
352 its wind data to also shed light on changes to wind patterns with location, although there is difficulty
353 differentiating these variations with seasonal variations if the same location has not been sampled multiple
354 times. A precedent exists only on Mars. The Curiosity rover traveled many kilometers from the bottom of
355 the northwest region of Gale crater towards Aeolis Mons, a feature of more than 5 km altitude at the center
356 of the crater. Along its traverse, the rover characterized the Bagnold Dune field around local winter in the
357 third Martian year of operations (Newman et al., 2017) and measured upslope winds during the daytime
358 getting stronger as it climbed Aeolis Mons (Viúdez-Moreiras et al., 2019a; 2019b).

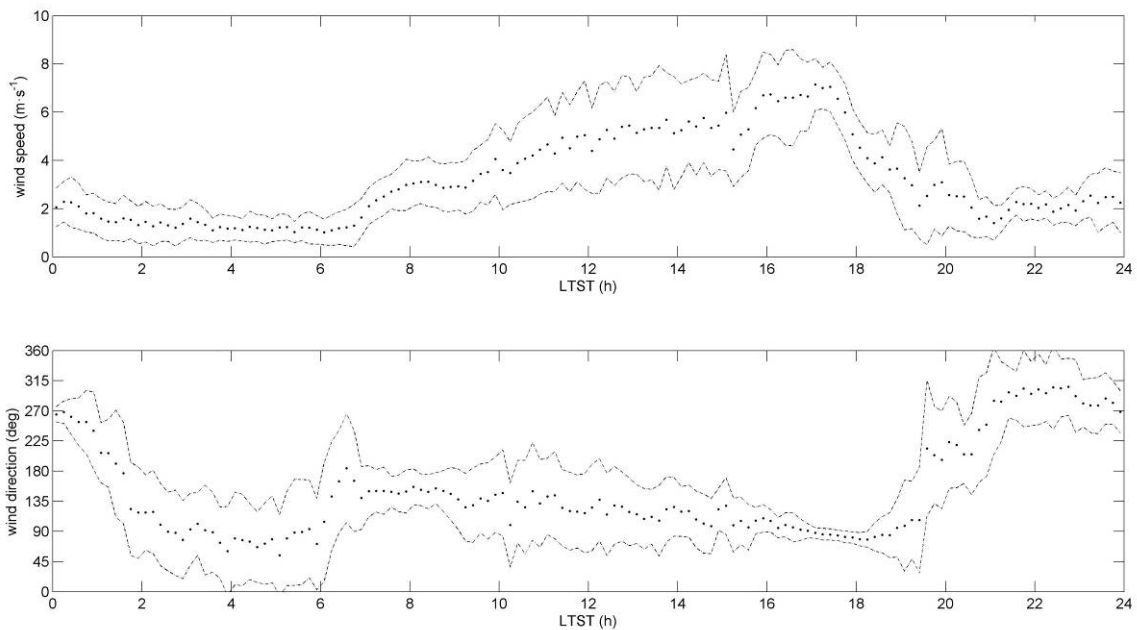
359 After exploring the delta remnant inside the crater, Perseverance will drive to the rim and out of Jezero,
360 likely driving to explore regions to the southwest. Different local dynamics are expected both closer to the
361 rim, where local downslope flows at night are expected to be much stronger, and outside the crater. In
362 addition, channeling effects and flow deviations closer to the crater rim and delta walls can be observed in
363 satellite images through analysis of the aeolian features (Fig. 4 bottom). This is particularly easy to observe
364 close to topographical features such as to the left of the mountain located to the west (hereafter M02-W,
365 Fig. 4 bottom). Focusing on Perseverance's trajectory, significant deviations from the prevailing winds can
366 be expected at least between sol 380 and 385 (where aeolian indicators suggest dominant west-
367 northwesterly winds instead of the prevailing west-southwesterly winds), and between sol 400 and 408
368 (where aeolian indicators suggest channeling effects by small-scale topography, and dominant
369 northwesterly winds, Fig. 4 bottom). After sol 410, the rover is very close to the delta walls (Fig. 4 top),
370 which may also imply disturbances in the observed winds. However, during the first 315 sols of the
371 mission, that is, the timescale currently covered by the wind sensor, the rover moved within a region of
372 only $\sim 1 \text{ km}^2$ (Fig. 4 bottom), in which strong variability neither in topography nor atmospheric dynamics is
373 expected. Therefore, we initially assume that the observed variability is due to the different temporal scales
374 and dust events.

375

376 4. DIURNAL VARIATION OF SURFACE WINDS AT JEZERO

377 4.1 Observed diurnal wind patterns

378 The Perseverance rover measured surface winds at Jezero during the first 315 sols of the mission, with
379 observations starting at sol 35 (Section 2). This corresponds to areocentric solar longitudes (L_s) from $\sim 22^\circ$
380 to $\sim 153^\circ$, i.e., much of northern spring ($L_s = 0 - 90^\circ$) and summer ($L_s = 90 - 180^\circ$).



381

382 **Fig. 5:** Diurnal variation in wind speed and direction as a function of local true solar time (LTST) over a
383 period of 40 sols close to the northern summer solstice. The direction from which the wind is blowing is
384 shown, following the standard meteorological convention. 10 min averages are shown as dotted line, with
385 the \pm one standard deviation shown in dashed lines.

386

387 The observed wind patterns at Jezero presented minor sol-to-sol variations that were generally
388 overwhelmed by the diurnal variations, in accordance with observations from previous missions on Mars
389 outside the dust storm season (e.g., Hess et al., 1977; Banfield et al., 2020). The acquisition strategy
390 involved in Mars 2020 operations (Section 2) prevented complete measurement of the diurnal cycle in a
391 single sol; therefore, multiple sols were necessary to fill the gaps, which were particularly of concern
392 during the afternoon due to more gaps at that time (Fig. 2). No major variability was observed in the
393 general shape of the diurnal cycle within the period of observation. Conversely, a mostly repeatable diurnal
394 cycle was measured, with minor long-term variability (detailed in the next subsection).

395 The observed diurnal cycle of winds presented two regimes: (i) a daytime or convective regime, from dawn
396 to sunset, with average easterly to southeasterly winds in which maximum wind speeds were measured, and
397 (ii) a nighttime regime with a period of W-NW winds followed by a relatively calm period until sunrise
398 with highly variable wind directions as a function of sol and time of night. In addition, two transition
399 periods occurred between the daytime and nighttime regimes. Fig. 5 shows the diurnal variation in wind
400 speed and direction, averaged in ten-minute windows over a period of 40 sols close to the northern summer
401 solstice, which is illustrative of the observed diurnal cycle throughout the first 315 sols of the mission.

402 Over this sol period, winds were southeasterlies during the morning when the PBL was developing. They
403 gradually rotated east as the day progressed, at the same time that wind speed strongly increased. Maximum
404 ten-minute-average wind speeds of $\sim 7 \text{ ms}^{-1}$ were measured during the late afternoon ($\sim 17 \text{ h LTST}$), when
405 winds were easterlies. This corresponds to the time of sol when the solar heating that drives daytime
406 upslope winds had lasted for several hours but was declining and would shortly be very low at sunset
407 ($\sim 18.5 \text{ h LTST}$). In addition, the wind variability, both in wind speed and direction, was strongly reduced in
408 the afternoon, when the PBL was fully developed and when turbulence was likely dominated by larger
409 eddies. Winds remained as east-northeasterlies in the afternoon while wind speed decreased abruptly at
410 17.5 h. After sunset, wind speeds continued decreasing whilst winds inverted the rotation that presented
411 throughout the daytime, rotating clockwise by a few degrees from east-northeasterlies to east-
412 southeasterlies from 18.5 h to 19.5 h. At 19.5 h, the daytime convective regime had ceased, and wind
413 speeds were weak, at $2 - 3 \text{ ms}^{-1}$. The winds then dramatically rotated clockwise from easterlies to west-
414 northwesterlies, between 19.5 h and 21.5 h. This rotation was coincident with a wind speed spike in some
415 sols that lasted for roughly an hour. Wind directions were then stable for ~ 2 hours with a slight shift
416 towards westerlies. After $\sim 21.5 \text{ h}$, wind speeds gradually increased, peaking with a local maximum around
417 midnight. A subsequent decrease produced the minimum wind speeds reached during the diurnal cycle, ~ 1
418 ms^{-1} , in a period characterized by a counter-clockwise rotation toward easterlies and with pronounced
419 variability in wind direction, comparable to that observed during the day. This period was characterized as
420 well by a strong sol-to-sol variability (see Section 5). Finally, half an hour after dawn ($\sim 5.5 \text{ h LTST}$), winds
421 rotated clockwise to S-SE and increased in intensity as the PBL developed, completing the diurnal cycle.

422 Notably, the observed variability represented in Fig. 5 by the standard deviation of wind speed and
423 direction as a function of LTST described above could, a priori, be due to both intrasol (sub-diurnal) and

424 intersol variations, given that 40 sols were averaged in this figure. Further analysis of such variability
425 shows that, in general, intrasol variability dominates during the daytime convective regime (turbulence
426 scale), while intersol variability dominates the ensembled multi-sol pattern during the night regime.

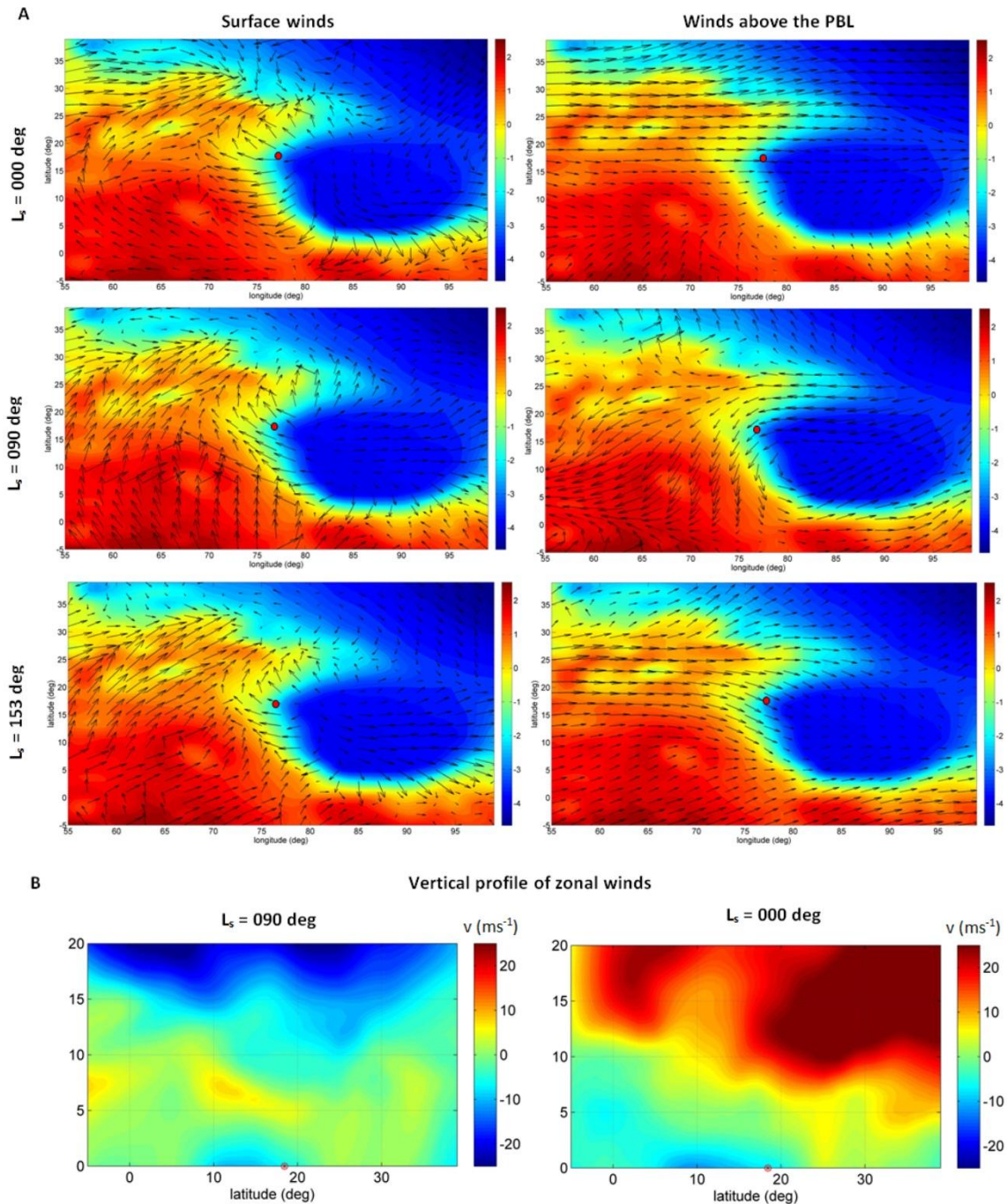
427 **4.2 Mechanisms affecting the diurnal cycle in the near-surface wind patterns**

428 The timing and magnitude of the observed regimes is consistent with control by slope flows. During the
429 daytime, mean wind direction matched the regional upslope of Isidis basin at Jezero region and the Jezero
430 crater rim slope (Fig. 4), although the wind direction shifted by $\sim 30^\circ$ north once the upslope winds were
431 fully developed in the late afternoon. This could be explained by upslope flows being perturbed by the
432 topography at Jezero region, together with the effect of local upslope flows. A full rotation of winds was
433 produced after sunset, when near-surface thermal gradients started to reverse after their daytime maxima.
434 Winds presented a similar orientation but in an opposite sense after rotation, i.e., at that time the wind
435 direction roughly matched the downslope of Isidis basin around the Jezero region and the crater rim slope.
436 The pre-landing general circulation model (GCM) and mesoscale simulations predicted strong control by
437 regional and/or local winds (Newman et al., 2021; Pla-García et al., 2021), consistent with the first
438 observations by Mars 2020 (Newman et al., 2022; Rodríguez-Manfredi et al., 2022). The modeled winds
439 usually ranged from northeasterlies to south-southeasterlies during the daytime, rotating to
440 westerlies/northwesterlies after sunset. The fact that the direction of the slopes of Isidis basin and Jezero
441 crater's western rim are similar makes discerning the mechanism that modulates the diurnal cycle at the
442 landing site difficult. Newman et al. (2021) suggested that largely similar wind patterns between the high-
443 and low-resolution simulations tested in the study during the daytime could indicate that the slopes of
444 Jezero crater, itself, cannot drive the winds during the daytime, as the local scale is not resolved in the latter
445 simulations. In any case, the low-resolution simulations may be shifting the daytime wind direction by
446 some degree, due to the variability in the Isidis basin slope direction at Jezero region (Fig. 3), thus
447 artificially mimicking the potential effect local anabatic winds have on the wind pattern. On the other hand,
448 given the small size of Jezero crater (less than 50 km), it is expected that upslope flows on the eastern crater
449 rim and on the mountain located close to the southeastern crater rim of Jezero (hereafter M01-SE, see Fig.
450 3) would act in opposition to the regional flow, consequently producing effects at the landing site location.
451 In that case, local forcing would produce complex constructive and destructive interactions in the near-
452 surface winds.

453 The gradual increase in wind speeds and the shift in wind direction as the daytime timeslot progressed can
454 be interpreted as the result of the gradual and different increase in the relative strength of regional and local
455 slope flows as the PBL develops, as reproduced in the model simulations to some extent. Therefore,
456 regional and local upslope flows would dominate during the daytime. Also, the importance of tidal flows
457 cannot be ruled out during the daytime. However, the complex structure of tidal flows and the weak diurnal
458 and semidiurnal tides at Jezero (Rodríguez-Manfredi et al., 2022), together with their representation in
459 models being sensitive to the three-dimensional dust distribution used, complicates discerning the relative
460 contribution of tidal flows under nominal conditions.

461 The vertical extent of the slope winds and the gradual coupling with winds aloft should also be considered.
462 The unstable daytime PBL present in the Martian atmosphere quickly transports momentum between the
463 near-surface and the atmosphere several kilometers above. Hess et al. (1977) attributed the behavior
464 observed by VL1 to a combination of near-surface slope flows, peaking in the mid-afternoon, and
465 maximum turbulent coupling with the winds aloft, peaking in late afternoon and acting constructively with
466 the former. In addition, analysis of the wind data acquired by the InSight Lander at Elysium Planitia
467 suggested that the reduction, or perhaps entire lack, of significant coupling during the nighttime could have
468 allowed downslope flows to develop, producing surface winds opposite to the strong winds from the
469 general circulation present during the northern summer in Elysium Planitia.

470 We performed MarsWRF GCM simulations in order to test the possible coupling of large-scale winds into
471 near-surface winds in the Jezero region, with the same version and setup successfully applied to previous
472 studies for the Gale crater region (Newman et al., 2017; Richardson & Newman, 2018; Viúdez-Moreiras,
473 2021), but using here only the global domain. We focused on the evaluation of the interference between the
474 large-scale and the regional slope winds on the northwestern slopes of Isidis basin, so it is not necessary to
475 resolve the local circulation at Jezero crater. These simulations show that surface winds on the slopes of the
476 Isidis basin are mostly insensitive to the higher winds in and above the PBL, due to the strength of daytime
477 slope flows on Isidis's slopes.



478
 479 **Fig. 6:** (A) Wind field at midday in the Isidis basin region from MarsWRF GCM simulations at northern
 480 spring equinox (top), summer solstice (middle) and at $L_s=153^\circ$ (bottom), averaging ± 5 sols. Surface winds
 481 and winds above the PBL (10 km) are shown in the left and in the right columns, respectively (see text). (B)
 482 Midday vertical profile of zonal winds at the landing site's longitude. Pseudo-altitude in km. The wind
 483 speed axis is constrained to ± 25 ms⁻¹ to better observe the range in Isidis basin. Jezero crater is shown by a
 484 red dot.
 485

486 The effect of mid-latitude westerly winds above the PBL can be observed outside summer (Fig. 6),
 487 indicated by the strong westerly circumpolar winds that reach the Isidis basin latitudes, and that are
 488 variably disturbed by tidal flows along the day. Within the jet streams, these winds can present velocities

489 greater than 100 ms^{-1} at high altitudes (Mitchell et al., 2015), and reach lower latitudes nearer the surface
490 with reduced wind speeds. Simulations presented in Fig. 6 show that the daytime PBL at Jezero's region is
491 subjected around the equinoxes to mid-latitude westerly winds that oppose the regional upslope near-
492 surface flows. These strong winds are slightly disturbed by tidal flows along the day. Conversely, around
493 the northern summer solstice these westerly winds are not present and winds above the PBL are dominated
494 by tidal flows, which act constructively to the near-surface winds during most of the daytime, particularly
495 during morning and midday. The vertical extent of the surface regional upslope winds produces even strong
496 winds at a couple of kilometers above the surface during the daytime (Fig. 6B). The PBL reaches in the
497 afternoon ~ 8 km at northern summer and ~ 5 km close to the equinoxes, achieving greater values at the fall
498 equinox than at the spring equinox. However, although the winds above the PBL can strongly affect the
499 high layers within the Isidis basin's PBL (Fig. 6B), simulations suggest that the effect on the surface winds
500 by the winds above the PBL is minor, even when winds above the PBL flow in opposite directions to the
501 surface winds (Fig. 6A), due to the intense daytime regional slope flows present in the Isidis basin's slopes.
502 Most of the slight differences observed in the near-surface patterns on the Isidis basin western slopes could
503 be attributed to the return branch of the Hadley cell. These results are in agreement with the weak southerly
504 shift in surface winds observed in several model pre-landing predictions for Jezero around southern
505 summer (Newman et al., 2021), which may be attributed to the Hadley cell circulation, although other
506 models do not present such a shift. It illustrates how the steep slopes of Isidis basin would be contributing
507 to isolation of the circulation from the large-scale dynamics in the Jezero region.

508 The nighttime regime presents several interesting features, with some differences from the daytime
509 scenario. An interesting feature is the effect of the nighttime PBL structure on the near-surface winds.
510 While the daytime PBL quickly transports and mixes momentum between surface and several kilometers of
511 height, the nighttime PBL is much shallower, maximizing the effect of small topographic features in their
512 surroundings that may reinforce mechanical turbulence in these areas and affect the downslope wind
513 intensity and direction. The Jezero region and Jezero crater itself contain significant topography (Fig. 2)
514 that could dramatically affect the nighttime patterns in the mesoscale ($\sim 10^2$ - 10^4 m) and in the microscale
515 (~ 10 s of m and smaller). The first part of the night, from sunset to 01 h LTST, was characterized by
516 relatively stable westerly/northwesterly winds that peaked around midnight as a likely result of downslope
517 winds peaking at that time. However, this is not what is expected from regional downslope flows, which

518 should peak right before sunrise, as the thermal conditions that drive katabatic flows (i.e., surface cooling
519 along slopes) grow overnight. Pre-landing atmospheric modeling from lower-resolution simulations (i.e.,
520 that did not resolve the topography of Jezero crater) predicted that regional slope flows at the Perseverance
521 landing site would, in general, grow during most of the night, reaching peak values shortly before sunrise
522 (Newman et al., 2021), which is not at all what is observed. Atmospheric modeling from higher-resolution
523 simulations (i.e., that did resolve the crater topography) predicted a spread of results, with the MarsWRF
524 modeling reproducing the observed peak around the midnight followed by a drop in wind speed to low
525 values by 02 h to 03 h. MarsWRF also shows that winds aligned with the Isidis basin downslope direction
526 are, on average, present across this general region at night, but are absent from the center of Jezero crater,
527 with the strongest winds (both in the crater and outside) instead linked to smaller-scale topography,
528 including strong downslope winds around the western crater rim. This supports the hypothesis that regional
529 downslope winds are weakened by the Jezero topography and that local downslope winds on the western
530 crater rim dominate during this timeslot (e.g., Newman et al., 2022).

531 After 01 h LTST, winds decreased in intensity and rotated counter-clockwise to variable directions,
532 although easterly winds dominate, with dramatic variability over most of the night (Fig. 5 and Fig. 7). This
533 reduction in the relative strength of the crater rim downslope winds was probably enhancing the effect of
534 another mechanism that was competing with the previous one. An analysis of the topography around the
535 landing site and the prevailing wind directions in this period indicate that the best candidates to provoke
536 such easterly flows should be the downslope winds at the eastern crater rim, possibly reinforced by
537 downslope flows on M01-SE. Such flows would compete with the western and other crater rim flows,
538 provoking convergent flows on the crater floor and periods of high mechanical turbulence and wind
539 variability. The nocturnal dynamics may also increase the likelihood of low-level jets at the nocturnal
540 inversion interface perhaps affecting the Perseverance's landing site in particular times (Pla-García et al.,
541 this issue). The very low wind speeds observed during this period of the night suggests that these
542 convergent flows are very weak or a destructive interaction around the landing site dominates the
543 atmospheric dynamics, provoking a calm region on the crater floor, at least at the Perseverance landing site.
544 The calm period observed in Jezero crater at night resembles what was observed in the early morning at
545 Gale crater, where the available data showed very low wind speeds (Viúdez-Moreiras et al., 2019a; 2019b)

546 probably driven by a similar mechanism (in that case due to downslope flows in Aeolis Mons and the
547 northern crater rims, greatly isolated from the regional and large-scale circulation).

548

549

550 **5. SOL-TO-SOL AND SEASONAL VARIABILITY IN WINDS**

551 **5.1 Potential mechanisms affecting the seasonal cycle in the near-surface wind patterns at Jezero**

552 The general circulation at the time of Perseverance's landing ($L_s \sim 5^\circ$) is characterized by a weak equinoctial
553 Hadley cell circulation, when the return branch of the northern cell would produce zonal-mean near-surface
554 northerly winds at Jezero's latitude. Thermal tides and planetary waves are also affecting the large-scale
555 circulation. In addition, strong westerly circumpolar winds aloft in the area reaching the PBL can be
556 observed in the simulations (Section 4.2 and Fig. 6).

557 The situation changes as the season progresses. Together with possible changes in the intensity of regional
558 and local slope flows, and seasonal variations in tides and planetary waves, the dual cell becomes a single
559 cell that is already developed by summer solstice ($L_s 90^\circ$) with upwelling (downwelling) at northern
560 (southern) mid-latitudes, producing near-surface southerly winds in the zonal mean. The effect of the
561 Hadley cell on surface winds is to a greater or lesser extent evident in the surface wind data of past
562 missions. Viking 1 data suggested a transition from regional topographic to global Hadley circulation
563 control of the winds above the landing site, with a remarkable effect on the surface winds measured by the
564 lander (Murphy et al., 1990). The MSL wind data confirmed model simulations that predicted the large-
565 scale, synoptic (>100 s of km in scale) flow has a much stronger influence at Gale Crater during the summer
566 and winter seasons when a single Hadley cell exists in the zonal mean (Rafkin et al., 2016; Newman et al.,
567 2017; Viúdez-Moreiras et al., 2019a). InSight data at Elysium Planitia indicated that the observed wind
568 patterns resulted from the interaction between regional and local slope flows induced by topography, which
569 all produced a diurnal perturbation superimposed on a mean flow, dominated by a combined effect of the
570 Hadley cell and channeling effects from the regional topography (Banfield et al., 2020; Viúdez-Moreiras et
571 al., 2020). However, although evident, the effect of meridional circulation in Mars 2020 wind data is
572 difficult to observe due to the dominance of regional and local slope flows and the lack of measurements in

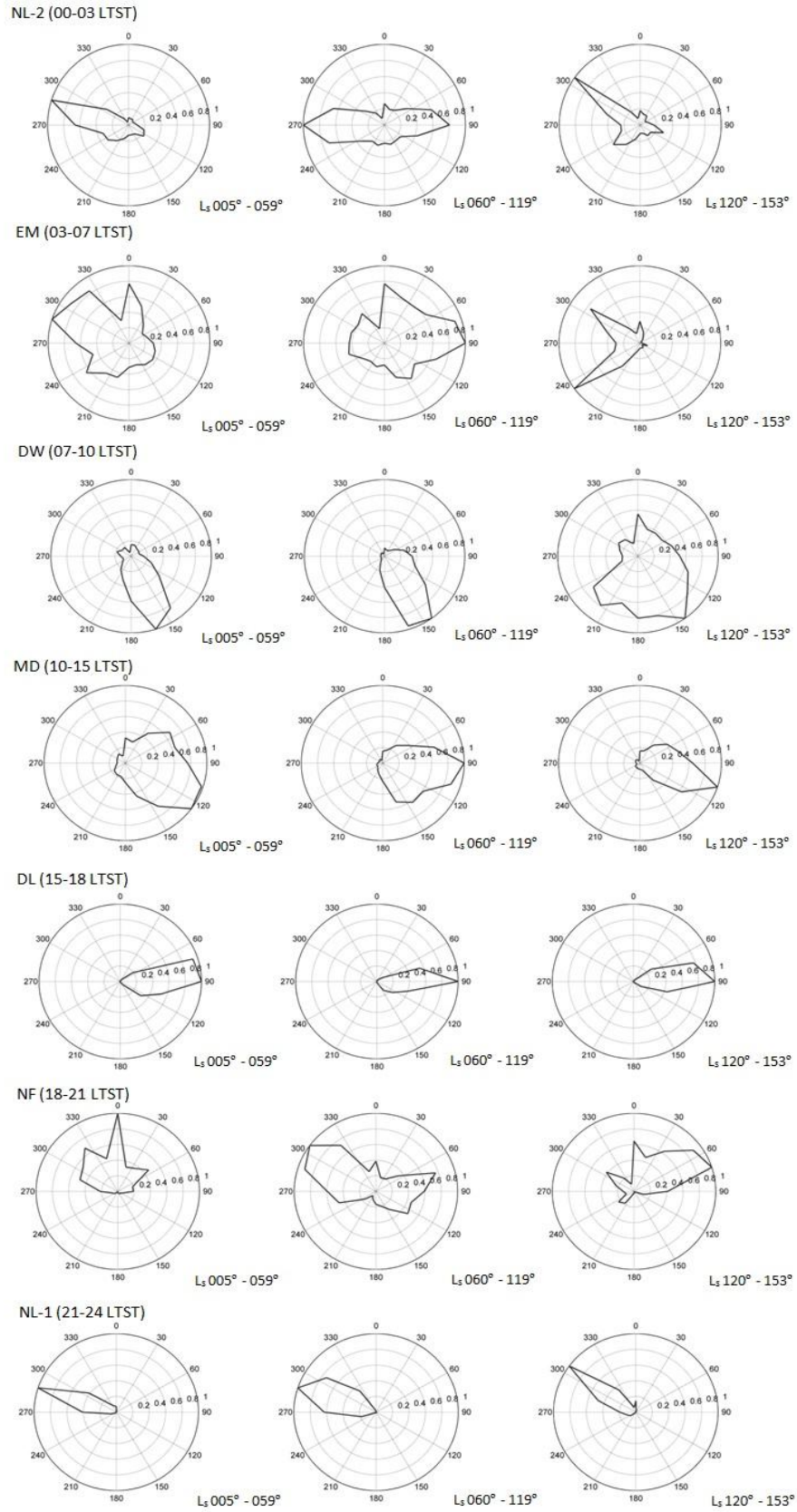
573 southern summer, the season when the mean meridional circulation is at its strongest (e.g., Richardson &
574 Wilson, 2002). Also, it is possible that the topography and variability in the terrain properties of this region
575 could be influencing the behavior of the meridional circulation from the zonal mean.

576 **5.2 Observed sol-to-sol and seasonal variability in daytime winds**

577 Fig. 7 presents the wind roses for three L_s ranges and seven periods of the day or diurnal timeslots. The
578 latter are chosen to combine hours with similar wind patterns, taking into account that the inherent
579 complexity of the surface wind patterns may imply variations within the diurnal timeslot, as we will
580 describe in that case. We use the same timeslots and nomenclature as presented in Viúdez-Moreiras et al.
581 (2019a; 2019b) for Gale crater. The diurnal timeslots are: (i) morning (DW), from 07:00 to 10:00 LTST,
582 (ii) midday (MD), from 10:00 to 15:00 LTST, (iii) afternoon (DL), from 15:00 to 18:00 LTST, (iv) night-
583 fall (NF), from 18:00 to 21:00 LTST, (v) night (NL-1), from 21:00 to 24:00 LTST, (vi) midnight (NL-2),
584 from 00:00 to 03:00 LTST, and (vii) early morning (EM), from 03:00 to 07:00 LTST. The time evolution
585 of wind speed and direction are presented in Fig. 8 for selected diurnal timeslots, similar to those used in
586 Fig. 7 but with slight modifications to allow for a better representation of the data as a function of season
587 given short-term data gaps present in certain periods.

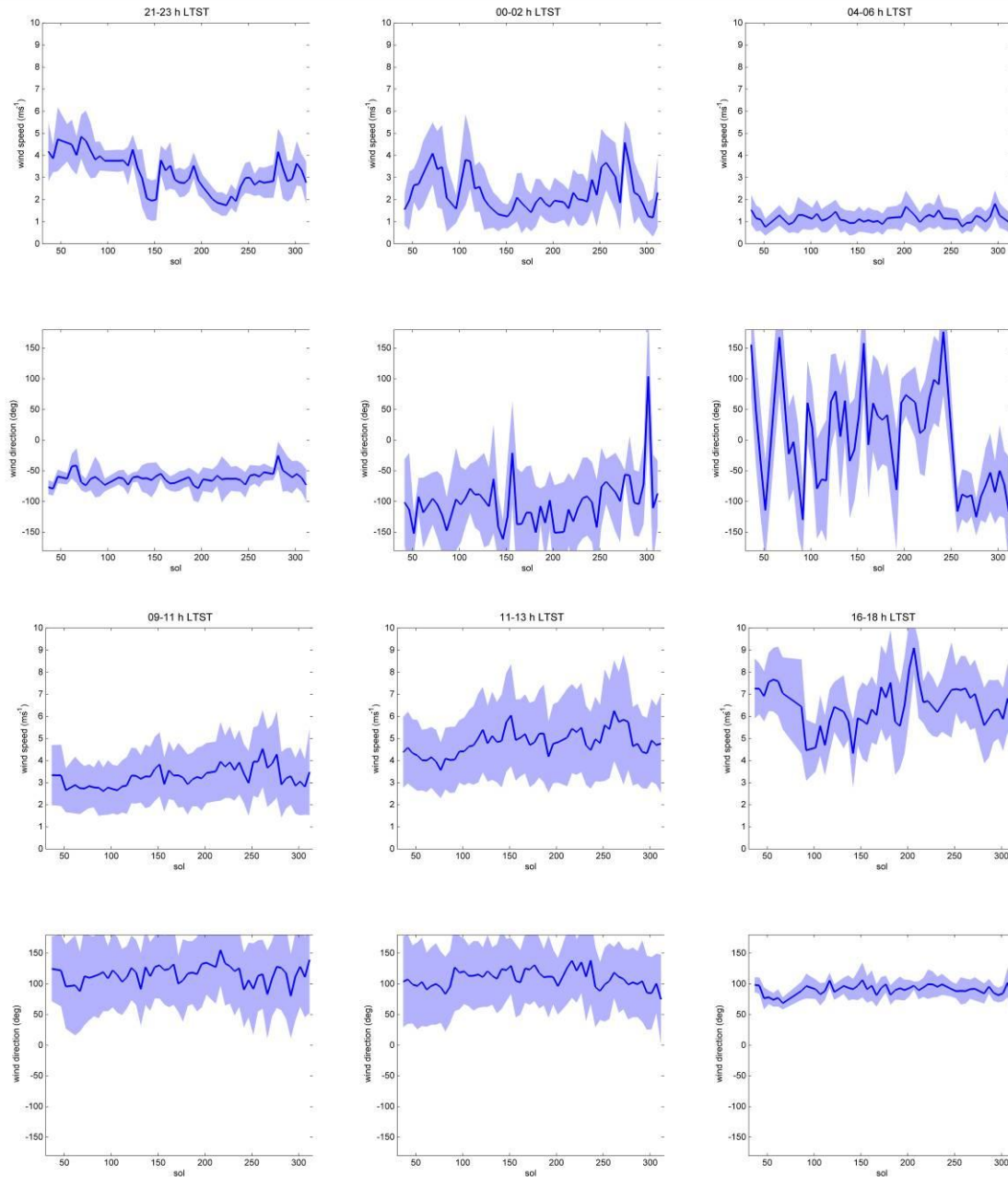
588 One-sol averages give more information about different dynamic processes that affect particular periods of
589 time, but the significant gaps involved in the wind data (particularly between 16-17 h and 16-18 h LTST in
590 the early sols of the mission) make it difficult to study the sol-to-sol variability systematically. Therefore,
591 5-sol average wind speeds and directions as a function of sol are presented in Fig. 8.

592 Overall, the seasonal variability for the winds observed by Mars 2020 between the northern spring and the
593 summer season was weak (Fig. 7), without dramatic variations, in agreement with the dominance of the
594 regional and local scales in the surface wind patterns (Section 3).



595
596
597
598

Fig. 7: Wind roses as a function of areocentric solar longitude (L_s) and time of the day until the wind sensor failure on sol 315 ($L_s \sim 153^\circ$). The direction from which the wind is blowing is shown, following the standard meteorological convention.



600 **Fig. 8:** Evolution in 5-sol average wind speeds and directions as a function of sol for different diurnal
 601 timeslots during the nighttime and daytime, with the \pm one standard deviation shown by the light blue
 602 shading.
 603
 604

605 During midday (MD diurnal timeslot in Fig. 7), when upslope winds were developing, prevailing
 606 southeasterly winds were measured during early spring. Significant sub-hourly variability was observed
 607 mainly due to turbulent scales (see the companion paper, part 2), which included measuring northeasterly
 608 and south-southeasterly winds at certain times. These variations overwhelmed intrasol and seasonal
 609 variations (Fig. 8). Over the summer solstice, prevailing winds turned to east and east-southeasterlies. The

610 seasonal variation of wind speeds peaked at that season (see the companion paper, part 2). During the
611 afternoon (DL diurnal timeslot in Fig. 7), the full development of regional slope flows overwhelmed the
612 effect of other potential mechanisms in the large-scale, maintaining roughly constant behavior in wind
613 directions as a function of season. The low variability in wind direction that characterized this timeslot,
614 probably due to the reduction in short term eddies as the PBL was fully developed (Section 4), was
615 maintained as a function of season.

616 The nightfall (NF) diurnal timeslot in Fig. 7 (18:00-21:00) is a period of transition between anabatic
617 upslope winds and katabatic downslope winds, and shows strong sensitivity to season. Counter-clockwise
618 rotation started in the first sols of the mission at ~18 h LTST (sunset at ~18.25 h LTST), with northerly
619 winds at 19.5 h LTST, and north-northwesterly winds at 22.5 h LTST as a result of local downslope winds
620 dominating at that time. As the mission progressed, the transition began later and occurred more rapidly.
621 Right before the summer solstice, the rotation was suddenly executed at 19 h - 19.5 h LTST (sunset at
622 ~18.5 h LTST). Right after the solstice, the sign reversed, that is, the rotation was performed clockwise and
623 the transition was very slow (Fig. 5). At mid-summer, the transition reversed again to counter-clockwise
624 rotation but with longer timescales typically observed in the first sols of the mission and beginning a bit
625 later. This seasonal behavior in the transition between upslope and downslope winds could be related to a
626 coupled effect of Hadley cell return flow and thermal tides. In fact, more southerly winds are expected as
627 approaching toward solstice, which is consistent with the change to a clockwise rotation. However, the
628 different behavior between pre-solstice and post-solstice would need the effect of another mechanism
629 acting together. As described, thermal tides produce variable tidal forcing as a function of time of day and
630 as a function of season. We observe significant changes in the phase of the diurnal pressure mode and also
631 a peak in the amplitude of the semidiurnal pressure mode after the summer solstice (Rodríguez-Manfredi et
632 al., 2022; Sánchez-Lavega et al., this issue). These changes suggest disturbances in tidal flows at that
633 season which could relate with the different behavior in the rotation at that period.

634

635 **5.3 Sol-to-sol and seasonal variability in nighttime winds**

636 West-northwesterly downslope winds were fully developed in the first part of the NL-1 timeslot in Fig. 7
637 (21-24 h LTST), which remained roughly constant throughout the mission and presented very little

638 variability in wind direction, similarly to that produced with the counterpart daytime upslope winds during
639 the afternoon. However, the longer rotation duration at midsummer from the daytime winds coincided with
640 a slight shift in the wind directions to northwesterly winds; that is, the local downslope winds had a greater
641 northerly component as the summer progressed. The intensity of midnight wind speeds, affecting the NL-1
642 and NL-2 timeslots, reduced to one half of the $4 - 5 \text{ ms}^{-1}$ observed at the beginning of the mission. Stable
643 atmospheric conditions during the night likely promoted the effect of topography on surface flows; and
644 significant topographic features in the surroundings such as the delta walls and crater rims, but also M02-W
645 (Fig. 4), could result in spatial differences in nighttime flow among rover locations as the mission
646 progressed. In fact, extreme shifts in wind direction can be inferred from aeolian signatures in the MRO
647 images close to the delta and in other topographical features (Fig. 4), with the delta walls producing what
648 appears to be a channel effect in the surface flows on the area (Section 3).

649 However, the observed variability as the mission progressed is mostly attributed to seasonal variations
650 (Section 3). It would include the effect of the large-scale circulation on the regional and local scale during
651 nighttime. Convergent local downslope flows on the crater floor during NL-1 and part of NL-2 were
652 probably competing, in the context of prevailing regional downslope flows from the west-northwest, and
653 with local downslope flows from the east-southeast likely reinforced by M01-SE. A single cross-equatorial
654 Hadley cell that develop around summer solstice would produce zonal-mean southerly winds near the
655 surface; these could compete with the slope flows, reducing the intensity of the regional downslope flows
656 in this region (northwesterly flows), in addition to local slope flows with such meridional and zonal wind
657 components, hence enhancing the effect of east-southeasterly local downslope winds. This situation would
658 reduce the strength of the northwesterly winds around midnight, as described earlier, and it was likely the
659 responsible for the winds from the east-southeast observed at the Mars 2020 landing site around the
660 summer solstice (Fig. 7, EM timeslot).

661 The second part of the night (NL-2 diurnal timeslot in Fig. 7, 00-03 h LTST) contains another transition in
662 which the intensity of the downslope winds in the crater rim decreased, starting a calm period extending as
663 late as the sunrise (Section 4). The NL-2 and EM diurnal timeslots in Fig. 7 involved the greatest wind
664 variability observed in the diurnal cycle, both in wind direction and in the relative wind speed variability
665 (see the companion paper, part 2). During the first sols of the mission, the local downslope flows reduced
666 their activity well enough to produce a counter-clockwise rotation towards easterlies at the end of NL-2.

667 Weak easterly winds developed in some sols at the end of this timeslot, while other sols had variable winds
668 during the calm period. Around summer solstice, the reduction in the intensity of downslope flows and the
669 subsequent rotation to easterly winds were more established, taking place in the middle/end of NL-2. After
670 L_s 120°, the situation was the reverse of that observed in the first sols of the mission. Some sols maintained
671 the downslope flows more often than others. This curious effect can be seen in Fig. 8 (00 – 02 h LTST).
672 The dramatic increases between sol 60 – 80 and between sols 110 – 120, as well as some periods between
673 sols 250 and 280, are the result of variable downslope flows that have an influence longer into the calm
674 period during the night and early morning (NL-2 and EM timeslots), and can be related to the lack of a
675 competing mechanism such as the Hadley cell circulation, which is present around the summer solstice.

676 The EM timeslot (03-07 h LTST) in Fig. 7 involved the greatest variability due to a combined effect of
677 intersol and intrasol variations. After L_s 120°, westerly winds developed again around 5 h LTST, but with
678 much less intensity than those observed at midnight, before the development of upslope winds in the
679 morning (see the DW, 07:00-10:00 LTST, timeslot in Fig. 7). As described above and in Section 4, these
680 rich nocturnal dynamics could result from downslope flows at the eastern crater rim, possibly reinforced by
681 downslope flows on M01-SE. Such flows, likely promoted around southern summer by the Hadley cell,
682 would compete with the western and other crater rim flows, provoking destructive interaction by
683 convergent flows on the crater floor, and periods with high mechanical turbulence and, hence, wind
684 variability. The dramatic seasonal rotation observed during this timeslot (Fig. 7) suggests large-scale
685 interference in the Jezero region circulation.

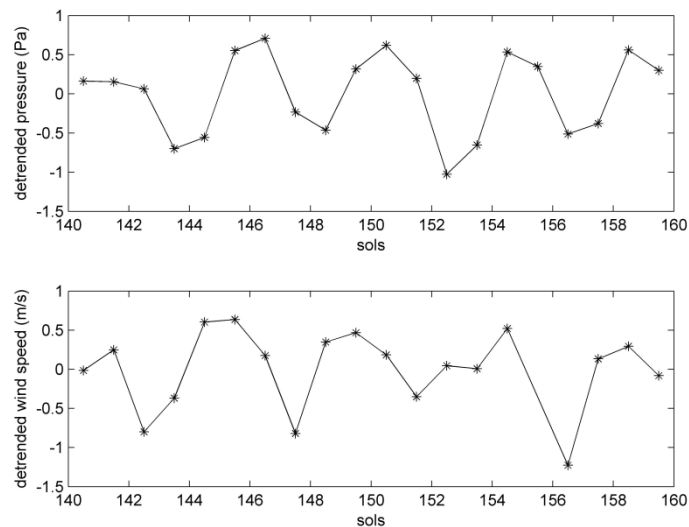
686
687
688

5.4 Atmospheric waves as a source of sol-to-sol wind variability

689 Most of the intersol variability is the result of stochastic variations produced by turbulence and interactions
690 with the different scales. However, part of the observed intersol variability in winds can be associated with
691 atmospheric travelling waves, possibly baroclinic. The effects of baroclinic waves were clearly observed in
692 the Viking Lander wind data, particularly by VL-2, which landed at 48°N, but also in VL-1, which landed
693 at 22.5°N (e.g. Barnes et al., 1980; 1984). These disturbances have also been observed in the InSight wind
694 data (Banfield et al., 2020), which landed in equatorial latitudes. Mars 2020 has detected travelling waves
695 in the pressure and temperature data (Battalio, 2021; Rodríguez-Manfredi et al., under review; Sánchez-

696 Lavega et al., this issue), with variable periods during the mission. MEDA wind data is constrained
 697 between $L_s \sim 22^\circ$ and $L_s \sim 153^\circ$ and have many gaps (Section 2) particularly in the first sols of the mission,
 698 which challenge the detection of travelling waves. After detailed analysis of the wind data, we are reporting
 699 the effects of travelling waves on the surface winds at Jezero.

700 There are several sol periods with a predominant period of oscillation; they are mostly weak and
 701 uncorrelated with pressure. However, a strong peak appears in the frequency analysis between sols 130 and
 702 170 both for wind and pressure variables, corresponding to waves of 4.4-sol period with $\sim 0.6 \text{ ms}^{-1}$
 703 amplitude both in wind speed and pressure. Fig. 9 shows the wind and pressure detrended signals (top and
 704 bottom, respectively) around sol 150 ($L_s \sim 75^\circ$, northern spring). This sol period is characterized by a clear
 705 harmonic in the signal. As noted, other sol periods show more variability and weak peaks in the wind
 706 spectra that are usually not well correlated with pressure. This could be influenced by the data gaps in the
 707 Mars 2020 wind data. However, given the gaps present in the data, it is expected that longer periods would
 708 also be affected by travelling waves.



709 **Fig. 9:** Detection of oscillations probably related to travelling waves in the Mars 2020 wind data. Detrended
 710 pressure (**top**) and wind (**bottom**) signals are shown around sol 150 (northern spring), after removing the
 711 subdiurnal variation related to thermal tides, regional/local flows and other mesoscale variations, and
 712 turbulence. In addition, seasonal variations such as those produced by the CO_2 cycle are removed as well.
 713 An oscillation period of ~ 4.4 sols is observed both in wind and pressure data.

714
 715
 716
 717
 718

6. EFFECTS OF THE MY36/2022 REGIONAL DUST STORM ON THE SURFACE WINDS

719 An early regional dust storm (RDS) affected Mars in January 2022 (MY36, $L_s \sim 153^\circ$). The storm passed
720 over Jezero crater on January 5 on mission sol 313, increased opacity to values greater than 1.5 on sols 314
721 – 317 from pre-storm values lower than 0.5, and persisted with variable opacities until sol 319 (Lemmon et
722 al., 2022; Smith et al., 2022). This event was the most intense observed by a surface mission since the
723 MY34/2019 large dust storm (LDS) that affected InSight’s landing site at Elysium Planitia and MSL’s
724 landing site at Gale crater (Viúdez-Moreiras et al., 2020c). However, the MY36/2022 storm duration (six
725 sols) was much shorter than the LDS duration (whose most noticeable disturbances ended a month after the
726 first effects were observed, and high levels of dust remained in the atmosphere for several sols, see Fig. 8 in
727 Viúdez-Moreiras et al., 2020c), more in agreement with the durations of typical regional dust storms.
728 Pressure tides and near-surface temperatures were strongly affected at the Perseverance landing site, similar
729 to what was observed during previous storms (e.g., Ryan & Henry, 1979; Zurek & Leovy, 1981; Wilson &
730 Hamilton, 1996; Lewis & Barker, 2005; Guzewich et al., 2016; Viúdez-Moreiras, 2019c; 2020c). However,
731 Perseverance was the first mission to make meteorological observations at a location with active storm dust
732 lifting; previous missions were either not located in active dust lifting centers, did not carry meteorological
733 sensors, and/or could not operate during a storm due to being solar powered. This enabled Perseverance to
734 study the strong aeolian activity (both dust lifting and sand motion) associated with the storm, including the
735 deposition of surface grains on the rover deck (Lemmon et al., 2022).

736 As described in Section 2, a close encounter with a dust devil on sol 313 at 13:42 LTST further damaged
737 WS2. Two sols later (sol 315 at 14:24 LTST), WS1 also experienced damage. The MEDA WS was
738 unavailable to provide wind data. The wind sensor was then kept off for several tens of sols, including over
739 the remaining storm period. However, wind changes during the onset of the storm at Jezero were able to be
740 measured.

741 Prior to the storm, on sols 310-311, the diurnal cycle of winds (Fig. 9) was similar to that observed
742 throughout the mission (Section 4), with the characteristic rotation between daytime and nighttime regimes
743 consistent with slope flow control. Winds were east-southeasterlies during the daytime, peaking in the
744 afternoon as usual, and then started to rotate progressively at ~ 17 h LTST towards westerlies. Between 20 h
745 and 21 h LTST, when winds were slowly rotating from upslope to downslope, strong winds developed with
746 wind speeds comparable to those measured in most of the daytime (but northerlies instead of the daytime’s
747 prevailing east-southeasterlies). This increase in wind speed after sunset was observed intermittently

748 throughout the mission, but was more pronounced after sol ~300. By contrast, nighttime winds were
749 weaker for sols 311-314 (Fig. 10).

750 On sol 312, the effects of the dust storm were clearly observed in the wind data, with southwesterlies
751 between 10 h and 11.5 h LTST rather than the usual southeasterlies observed, i.e., the zonal winds were
752 opposite in direction to those observed under nominal conditions (outside the dust storm). Winds abruptly
753 rotated to southeasterlies at 11.5 h and remained mostly as usual in the afternoon. On sol 313, the
754 disturbances were more dramatic, with a smooth clockwise rotation from southwesterlies to easterlies
755 between 10 h and ~14 h LTST, and with stronger wind speeds than usual over this period, comparable to
756 the peak speeds typically measured later in the afternoon. Due to the damage to WS2 at that time, which
757 caused the WS to turn off for several sols, no wind data were taken during the afternoon under storm
758 conditions; hence the peak wind speeds during the storm may not have been captured. At night, the data
759 extracted from the remaining operating boom suggested that downslope westerly flows were much more
760 intense than under nominal conditions, reaching 7 ms^{-1} at midnight.

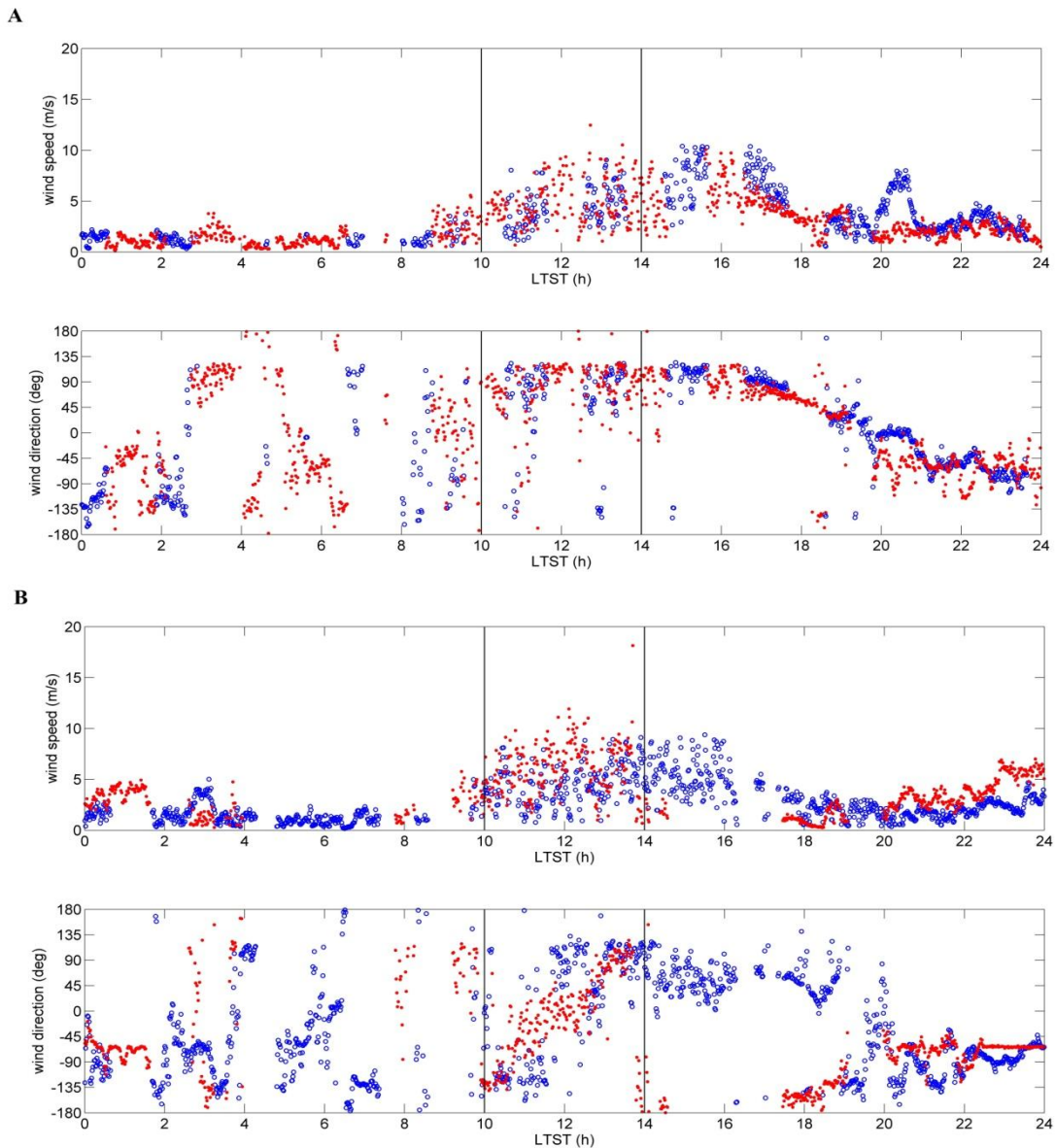
761 Changes to the surface wind pattern during a dust storm can arise from several different mechanisms, as
762 discussed, e.g., in Viúdez-Moreiras et al. (2020). First, a dust storm can locally (or even
763 regionally/globally) modify the atmospheric static stability (e.g., Zurek, 1976) and thus the coupling
764 between winds aloft and near the surface. Second, once the dust storm has grown enough (this will also
765 depend on its location) that it influences the large-scale pattern of solar heating, it can enhance the strength
766 of the zonal mean meridional (Hadley cell) global circulation (Basu et al., 2006; Heavens et al., 2011; Kass
767 et al., 2016). Third, and typically at the same stage of growth as in the latter case, it can increase the
768 strength of thermal tides and thus tidal flows (e.g., Zurek & Leovy, 1981; Wilson & Hamilton, 1996).
769 Indeed, such tidal enhancement has been linked to the broadening and strengthening of the summer solstice
770 Hadley cell (Wilson & Hamilton, 1996).

771 At L_s 153° , the Hadley cell is transitioning from the solstitial southern winter cell to a weak, dual cell,
772 equinoctial circulation. Simulations with the MarsWRF GCM for $L_s \sim 153^\circ$, presented in Fig. 6, show,
773 without the effects of a dust storm, surface winds fully driven by regional slope flows on the Jezero region
774 in the Isidis basin slopes (the simulations do not resolve Jezero crater, which presents similar local slopes at
775 Perseverance's location (W vs. NW), hence, a similar direction in the daytime anabatic winds). Simulations

776 suggest that winds above the PBL are northwesterlies on average on the Isidis basin northwestern slopes
777 throughout these sols, opposing the near-surface slope flows. These results are not consistent with dust
778 storm observations, which suggest a mechanism producing high wind speeds instead of acting
779 destructively. The observed clockwise rotation around noon from southwesterlies to easterlies between 10 h
780 and ~14 h LTST in sols 312 and 313 is also inconsistent with an enhanced Hadley cell circulation, which
781 should promote a particular meridional component in surface winds, instead of variable northerlies or
782 southerlies separated by a few hours. Conversely, changes are in agreement with what is expected by
783 thermal tides, as was observed in previous storms. Thus, enhanced tidal flows likely affected the surface
784 wind patterns at Jezero, producing a dramatic clockwise rotation from southwesterlies to easterlies around
785 midday and in less than 4 hours. In fact, thermal tides were strongly affected during the dust storm. Both
786 the diurnal and the semidiurnal pressure modes were doubled between sols 310 and 313, driving higher
787 diurnal pressure amplitudes during this period. The changes included dramatic disturbances in phase, as is
788 usual during these events (e.g., Ryan & Henry, 1979; Leovy & Zurek, 1979; Zurek & Martin, 1993). The
789 further deviation in the nominal wind patterns as diurnal and semidiurnal modes enhance and storm
790 progresses supports this hypothesis.

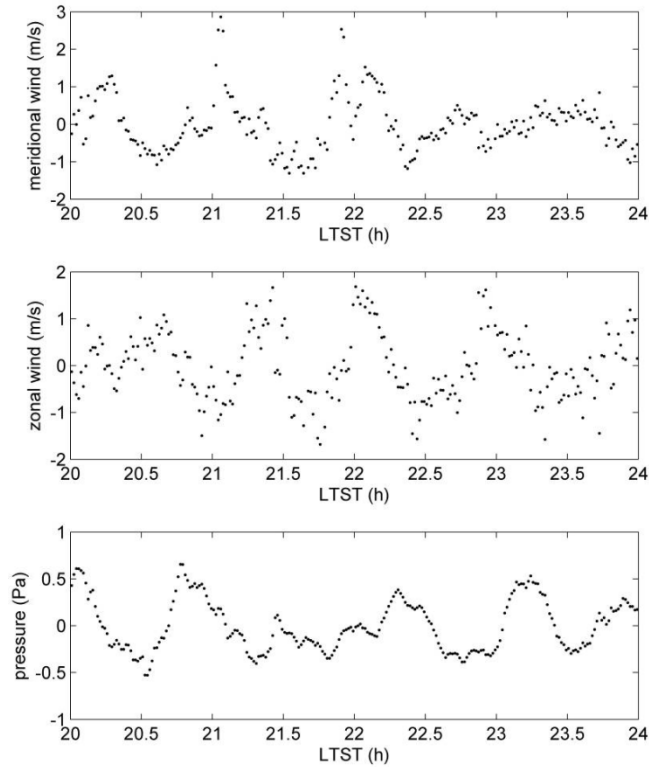
791 The nighttime regime in sols 311 - 313, before the calm period, was affected by significant low-frequency
792 oscillations (Fig. 10 and Fig. 11), probably due to gravity waves. These oscillations were observed after the
793 sunset, when downslope winds developed, and remained until midnight, with periods of 50 ± 10 min, and
794 $\sim 0.75 \pm 0.25$ m/s of amplitude in the zonal and meridional components of surface winds, with a small
795 counterpart in pressure (~ 0.5 Pa) and temperature (~ 1 K) perturbations. Winds were, at that time, west-
796 northwesterlies on sol 311, west-southwesterlies on sol 312 and west-northwesterlies on sol 313.
797 Oscillations were better observed on sol 313 and in the zonal winds, likely as a result of the detrending
798 procedure and the small relative uncertainties in the zonal component of surface winds (Fig. 11). On that
799 sol, there was a ~ 15 min shift in the zonal and meridional signals, that is, they were $\sim 90^\circ$ out of phase,
800 while the phase difference between winds and pressure was $\sim 180^\circ$. The relatively long period of these
801 waves suggests that the origin is not local. Neglecting Coriolis forces and assuming a linear relationship
802 between wind and pressure perturbations at first order (Coleman & Knupp, 2010; Banfield et al., 2020), the
803 phase speed, c , can be computed by $c = u + P' / (\rho \cdot u')$, where u is the wind speed, ρ is the atmospheric
804 density and P' and u' are the pressure and wind perturbations, respectively. It leads to phase speeds of 26-

805 28 ms^{-1} and horizontal wavelengths of 70-90 km. Therefore, we suggest that the origin of these waves may
806 be the slopes of Isidis basin, possibly due to topographical effects or wind shear between regional
807 downslope winds and the general circulation disturbed by enhanced tidal flows. The enhancement of the
808 wave activity during the MY36/2022 regional dust storm at Jezero agrees with data from previous missions,
809 which showed near-surface wave activity enhancement in dust storm periods (Banfield et al., 2020;
810 Guzewich et al., 2021). Gravity waves have a strong relevance for atmospheric dynamics including mixing
811 of energy, momentum and species in the very stable Martian nighttime PBL during dust storm conditions,
812 as well as in the thermal structure of the atmosphere and, hence, in circulation (e.g., Barnes, 1980; Fritts &
813 Alexander, 2003; Heavens et al., 2020 and references therein).



814

815 **Fig. 10:** Wind speed and direction (1 min averages) for (A) sols 310 and 311 (pre-storm conditions; in blue
 816 and red, respectively) and (B) sols 312 and 313 (storm onset at Jezero; in blue and red, respectively).
 817 Vertical lines show 10:00 and 12:00 LTST delimiting the period where the tidal winds were likely to
 818 produce the major change in winds during the storm. The direction from which the wind is blowing is
 819 shown, as in Fig. 5, following the standard meteorological convention; although here in a [-180,180] range
 820 to better visualize the wind rotation at sol 313.
 821
 822



823 **Fig. 11:** Waves observed at night during the regional dust storm, while downslope flows developed in Isidis
 824 basin and Jezero crater. Time evolution is shown as a function of local true solar time (LTST). Both
 825 pressure and wind were detrended subtracting a running average of $4 \cdot 10^3$ s from 1-min average signals.
 826
 827
 828

829 Sols 314 and 315, before the further damage to the WS, were mostly lost in terms of data, which was
 830 operating with only one working WS boom (pointing toward the front of the rover) and was a period when
 831 the rover heading was to the southwest, meaning that the remaining boom was unable to capture the
 832 prevailing daytime winds. However, the available data suggest that morning winds continued to be
 833 southwesterlies, as on sol 313, with maximum minute-averaged wind speeds close to 8 ms^{-1} , in agreement
 834 with previous sols. Nighttime downslope winds appeared to develop on sol 314 as usual, although the
 835 available data prevents knowing if wave activity occurred as in previous sols.

836 Wind speeds deserve a special mention. Summarizing what was observed regarding wind speeds during the
 837 onset of the storm at Jezero, mean winds appeared to be slightly greater during the storm than in pre-storm

838 conditions. On the other hand, vortex activity strongly increased during the storm, particularly in early
839 stages (Lemmon et al., 2022), and provoked a higher probability of close encounters. One of these
840 encounters at sol 313, 13:42 LTST, produced an intense wind gust that damaged the wind sensor. This gust
841 can be seen in Fig. 10 in the two measurements that depart from the average on sol 313. The companion
842 paper (part 2) will detail this event.

843 As described, no wind data are available after sol 315 (L_s 153°) and, therefore, there is no direct
844 information on wind patterns after the storm. Model simulations predict similar behavior in near-surface
845 wind patterns as the season progresses (Newman et al., 2021; Pla-García et al., 2021); they differ, in
846 general, only in the strength of daytime and nighttime winds (with daytime winds being weaker in the
847 northern winter). However, the modeled wind directions are mostly unaffected, showing easterly and south
848 easterly winds at midday.

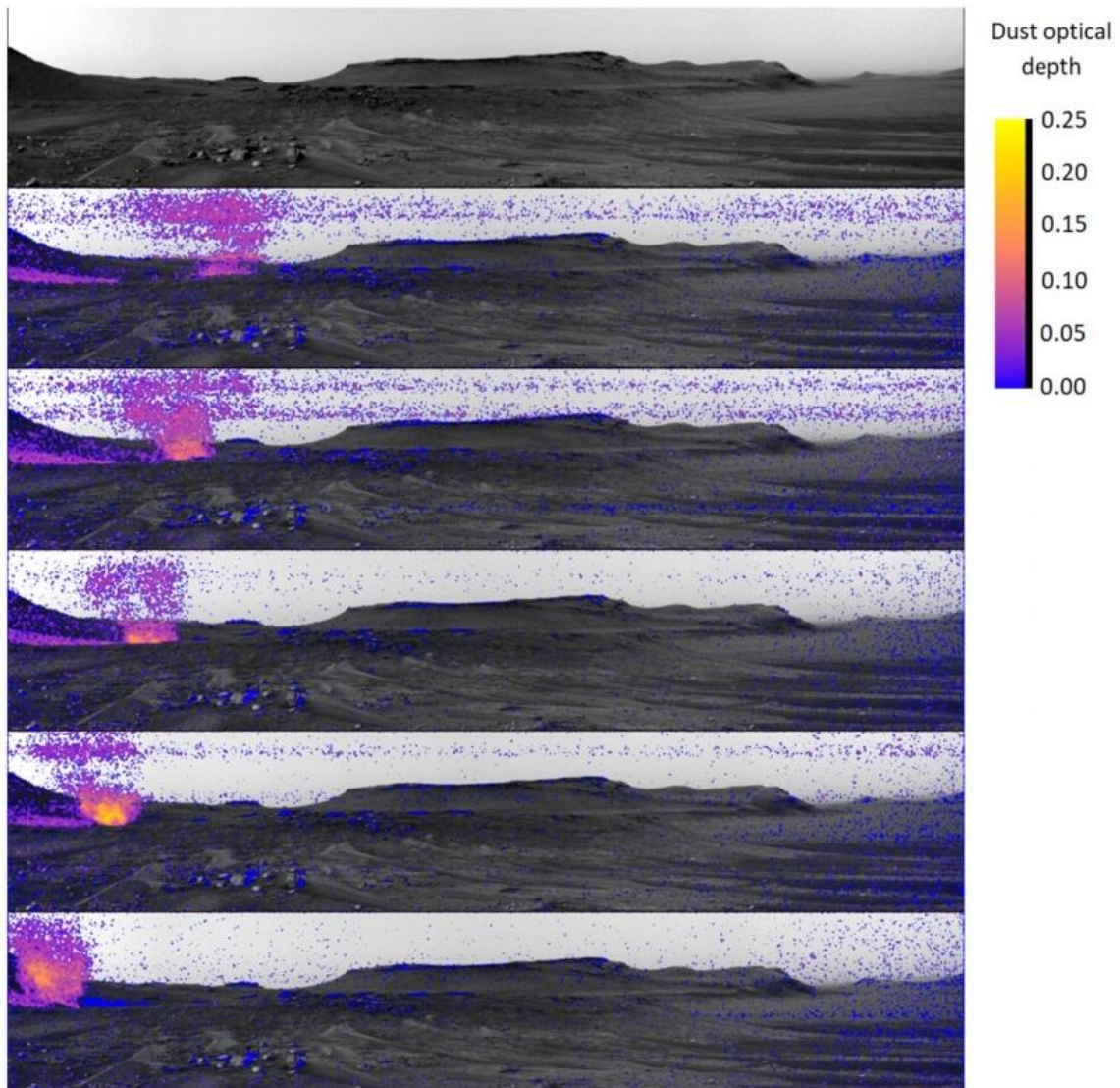
849

Mission sol	L_s (deg)	LMST (h)	Event notes	Inferred background wind direction (deg)
323	157.9	12:50		90 ±30
327	160	12:33		135 ±15
347	170.9	12:42	The apparent motion is slight toward 305 with wobbling	125 ±15
362	179.5	15:38		100 ±20
364	180.6	12:20	Slight movement	160 ±30
365	181.2	13:08		135 ±45
368	183	12:04		90 ±45
370	184.1	11:37	Dust devils seem to converge and get closer	10 ±15
372	185.3	11:40	Multiple dust devils move away from rover	10 ±15
373	185.9	11:56		180 ±30
373	185.9	11:58	Slight movement	150 ±15
380	190	15:50	Very distant dust devils	indeterminate
383	191.8	11:40	Very distant dust devils	indeterminate
407	206.5	15:00	Sense of movement is uncertain	60 ±30 or 240 ±30
425	217.7	13:40	Nearby DD	65 ±15
472	248.1	12:25	Distant dust devil and nearby dust cloud move toward rover	120 ±15
473	248.7	12:07	Two distant dust devils converge	120 ±15

850

851 **Table 2:** Inferred wind direction from dust lifting events detected in Navcam surveys or movies. Mission
852 sol, areocentric solar longitude (L_s), local mean solar time (LMST) and event notes are included together
853 with the inferred background wind direction. The direction from which the wind is blowing is shown,
854 following the standard meteorological convention.
855

856
857



858
859
860
861
862
863
864

Fig. 12: Enhanced color images for the event at sol 425, corresponding with a dust devil moving WNW, 300 ± 20 m away the rover, at 5.2 ± 0.5 m/s. Dust optical depth is included. Delta walls are likely affecting background winds at that location, leading to west-northwesterly winds.

865
866
867
868
869
870
871

As described in Section 2, in the absence of a working wind sensor, surface winds may be inferred, under particular conditions, from other sensors and/or from their interaction with surface. We have attempted to obtain some information on surface winds from dust devil Navcam surveys or movies after the wind sensor damage. The wind direction estimations, acquired around noon local time or shifted to the afternoon, are presented in Table 2. It was possible to infer the DD trajectory in 15 events, from sol 323 (L_s 158°) to sol 473 (L_s 249°). The only reported events to have well-constrained distance and radial motion were on sol 425 and 472: the first, shown in Fig. 12, was a 32 ± 3 m diameter dust devil moving WSW, 300 ± 20 m away, at 5.2 ± 0.5 m/s; the second was a 20-40 m length gust on sol 472 moving WNW at 14 ± 4 m/s. The surveys

872 showed diurnal wind directions that are consistent with the MEDA data before sol 313 and with the model
873 simulations. On average, wind directions were southeasterlies around the fall equinox and easterlies at
874 autumn, with significant deviations probably due to the daytime turbulence, mainly around the fall equinox.
875 These empirical results confirm that winds continued to be slope-driven during the late summer and fall
876 seasons. Additionally, it is likely that the topography affected the background wind patterns as the rover
877 approached the delta walls (Section 3), as can be seen in the winds inferred from surveys near sol 400,
878 which lead to west-northwesterly winds. It opens the possibility of expanding our knowledge of surface
879 wind patterns with other wind indicators as the mission progresses, thus complementing the wind sensor
880 data.

881
882
883

7. SUMMARY AND CONCLUSIONS

884 This paper presents the observed wind patterns at Perseverance's landing site, on the Jezero crater floor
885 close to the delta of an ancient river. The contemporaneous wind measurements in Jezero have also
886 supported the first flights of an unmanned aerial vehicle, the Ingenuity helicopter, on Mars.

887 The observed wind patterns at Jezero presented minor sol-to-sol variations generally overwhelmed by
888 diurnal variations, in accordance with observations by previous missions on Mars outside the dust storm
889 season. No significant variability was observed in the general shape of the diurnal cycle during the
890 observation period. Conversely, a mostly repeatable diurnal cycle was measured and presented two
891 regimes: (i) a daytime or convective regime, from dawn to sunset, with average easterly to southeasterly
892 winds and where maximum wind speeds were measured, and (ii) a nighttime regime with a period of
893 westerly/northwesterly winds followed by a period of relative calm until sunrise with highly variable wind
894 directions as a function of sol and time of night. The timing and magnitude of the observed regimes is
895 consistent with control by slope flows.

896 The fact that the slopes of Isidis basin and the Jezero crater western rim have a nearly similar direction
897 complicates the discernment of which mechanism is modulating the diurnal cycle at the landing site.
898 During the daytime, the gradual increase in wind speeds and the shift in wind direction as the daytime
899 timeslot progressed can be interpreted as the result of the gradual and different increase in the relative
900 strength of regional and local slope flows. During the night, the thin PBL depth maximizes the effect of

901 smaller topographic features near the rover, therefore affecting the intensity of the regional-scale
902 downslope winds in these areas and increasing mechanical turbulence. The Jezero region and the crater
903 itself present significant topography that could dramatically affect the nighttime patterns in the mesoscale
904 and in the microscale. The first part of the night, from sunset to ~01 h LTST, was characterized by quite
905 stable westerly/northwesterly winds, peaking around midnight as a likely result of downslope winds
906 peaking at that time, which is reproduced by pre-landing simulations. After ~01 h LTST, winds decreased
907 in intensity and rotated counter-clockwise to roughly easterlies, with a dramatic variability during most of
908 the nighttime. This reduction in the relative intensity of the crater rim downslope winds at the rover's
909 location would enhance the effect of competing mechanisms, likely downslope winds at the eastern crater
910 rim reinforced by downslope flows on M01-SE. The great sub-diurnal and sol-to-sol variability observed
911 by Mars 2020 was consistent with an increase in mechanical turbulence caused by these convergent flows
912 on the crater floor. The very low wind speeds observed during the early morning suggests that these flows
913 were very weak and/or that a destructive interaction around the landing site was dominating the
914 atmospheric dynamics, inducing a calm region on the crater floor.

915 Data suggest that the surface circulation at Jezero is highly unaffected by large-scale circulation, except
916 during particular periods in the diurnal cycle or, more generally, during dust storms conditions. As a result,
917 the seasonal variability for the winds observed by Mars 2020 between the northern spring and the summer
918 season was weak, without dramatic variations. However, sol-to-sol and seasonal effects were observed by
919 Perseverance rover, most of them at periods during the night. One of these particular periods in the diurnal
920 cycle is the transition from daytime to nighttime. In the first sols of the mission, the transition from daytime
921 to nighttime wind directions involved a counter-clockwise rotation, but this reversed to a clockwise rotation
922 as the mission progressed. The duration of the transition was also long close to the equinoxes, lasting
923 several hours, and sharp around the summer solstice. This seasonal behavior in the transition between
924 upslope and downslope winds could be related to a coupled effect of Hadley cell return flow and thermal
925 tides. Between 20 h and 21 h LTST, when winds were slowly rotating from upslope to downslope, strong
926 winds developed, producing sometimes wind speeds comparable in some cases to those measured in most
927 of the daytime, but with different directions from the prevailing southeasterlies. Also, nighttime downslope
928 flows lasted variable durations. After peaking at midnight, they intermittently reached Perseverance's
929 location in some sols of the mission, and in others the calm period was present earlier. During this

930 nighttime period and in early morning, seasonal variations suggest large-scale interactions with the regional
931 and local circulation.

932 Although the sol-to-sol variations were weak on average, travelling wave activity was observed on surface
933 winds at Jezero. A strong peak appeared between sols 130 and 170, corresponding to waves of 4.4 sol
934 period and $\sim 0.5 \text{ ms}^{-1}$ of amplitude in wind speed. Given the gaps present on the Mars 2020 wind data, it is
935 expected that longer periods would also be affected by baroclinic instability.

936 An early regional dust storm (MY36/2022) affected Mars on January 2022 ($L_s \sim 153^\circ$). The optical depth in
937 Jezero crater showed significant effects on sol 313. A close encounter with a dust devil on this sol damaged
938 the wind sensor, and further damage on sol 315 meant that no wind data are available for the remaining
939 storm period. However, the onset of the storm at Jezero was captured, and showed dramatic perturbations
940 in wind directions compatible with tidal flows produced by enhanced thermal tides, and increased wind
941 speeds both during day and night. The nighttime regime on sols 311 - 313 was affected by significant low-
942 frequency oscillations, suspected to be from gravity waves. The relatively long period of these waves
943 suggests that the origin is not local. We suggest that the origin of these waves may be the slopes of Isidis
944 basin, possibly due to topographical effects or wind shear between regional downslope winds and the
945 general circulation disturbed by enhanced tidal flows. The enhancement of wave activity during the
946 regional dust storm at Jezero agrees with results of previous missions and is highly relevant for atmospheric
947 dynamics including mixing of energy, momentum and species in the nighttime PBL during dust storm
948 conditions.

949 There are no wind data after the storm at $L_s 153^\circ$. In the absence of a working wind sensor, surface winds
950 may be inferred, under particular conditions, from other sensors and/or from their interaction with surface.
951 We have attempted to obtain some information on surface winds from dust devil movies (DDMs) taken by
952 the rover's cameras. On average, wind directions were southeasterlies around the fall equinox and easterlies
953 in autumn. These empirical results confirm that winds continued to be slope-driven during the late summer
954 and fall seasons, opening the possibility of extending the wind dataset with other wind indicators as the
955 mission progresses. Additionally, it is likely that the topography affected the background wind patterns as
956 the rover approached the delta walls.

957

958

DATA AVAILABILITY AND OPEN RESEARCH

959 The data used in this work are publicly available in the NASA's Planetary Data System (PDS)
960 (<https://pds.nasa.gov/>).

961

ACKNOWLEDGMENTS

962 The authors acknowledge and thank the Mars 2020 team. This work is supported by the Spanish Ministry
963 of Science and Innovation, under project RTI2018-098728-B-C31. Part of the research was carried out at
964 the Jet Propulsion Laboratory, California Institute of Technology, under a contract with the National
965 Aeronautics and Space Administration (80NM0018D0004). The UPV/EHU team is supported by Grant
966 PID2019-109467GB-I00 funded by 1042 MCIN/AEI/10.13039/501100011033/ and by Grupos Gobierno
967 Vasco IT1742-22.

968

REFERENCES

- 969 Balaram, J., Aung, M. & Golombek, M.P. The Ingenuity Helicopter on the Perseverance Rover. *Space Sci*
970 *Rev* 217, 56 (2021). <https://doi.org/10.1007/s11214-021-00815-w>
- 971 Balme, M., Greeley, R., (2006). Dust devils on Earth and Mars. *Rev. Geophys.* 44, RG3003.
972 <http://dx.doi.org/10.1029/2005RG000188>.
- 973 Banfield, D., Spiga, A., et al. (2020) The atmosphere of Mars as observed by InSight. *Nat. Geosci.* 13, 190–
974 198. <https://doi.org/10.1038/s41561-020-0534-0>
- 975 Barnes, J. R. (1990) Possible effect of breaking gravity waves on the circulation of the middle atmosphere
976 of Mars. *J. Geophys. Res.* 95, 1401–1421.
- 977 Basu, S., Wilson, J., Richardson, M., and Ingersoll, A. (2006), Simulation of spontaneous and variable
978 global dust storms with the GFDL Mars GCM, *J. Geophys. Res.*, 111, E09004, doi:10.1029/2005JE002660
- 979 Battalio, J.M. (2021) Baroclinic Traveling Waves Detected by Mars 2020 MEDA, AGU Fall Meeting
980 2021, abstract P25A-01, New Orleans, LA.
- 981 Bell et al. (2022) Geological and Meteorological Imaging Results from the Mars 2020 Perseverance Rover
982 in Jezero Crater, *Science advances*, under review.
- 983 Charalambous, C., et al. (2021) Vortex-dominated aeolian activity at InSight's landing site, Part 1: Multi-
984 instrument observations, analysis and implications. *J. Geophys. Res.* 126, e2020JE006757 doi:
985 10.1029/2020JE006757
- 986 Coleman, T. A. & Knupp, K. R. (2010) A nonlinear impedance relation for the surface winds in pressure
987 disturbances. *J. Atmos. Sci.* 67, 3409–3422.

988

- 989 Etiope, G., & Oehler, D. Z. (2019). Methane spikes, background seasonality and non-detections on Mars: A
990 geological perspective. *Planetary and Space Science*, 168, 52– 61.
- 991 Farley, K.A., Williford, K.H., Stack, K.M. et al. Mars 2020 Mission Overview. *Space Sci Rev* 216, 142
992 (2020). <https://doi.org/10.1007/s11214-020-00762-y>
- 993 Forget, F., Banfield, D., Millour, E., Spiga, A., Newman, C., Viúdez-Moreiras, D., Pla-Garcia, J., Navarro,
994 S., Mora-Sotomayor, L., Torres-Redondo, J., Rodriguez-Manfredi, J. A., Lewis, S., Lorenz, R., Lognonne,
995 P., & Banerdt, B. (2019). Mars large scale meteorology observed by InSight. Paper presented at EPSC-DPS
996 Joint Meeting 2019, EPSC-DPS2019–903.
- 997 Fritts, D. C. & Alexander, M. J. (2003) Gravity wave dynamics and effects in the middle atmosphere. *Rev.*
998 *Geophys.* 41, 1003.
- 999 Gomez-Elvira, J., Armiens, C., Castaner, L., Dominguez, M., Genzer, M., Gomez, F., Haberle, R., Harri,
1000 A.M., Jimenez, V., Kahanpää, H., Kowalski, L., et al. (2012). REMS: the environmental sensor suite for the
1001 Mars Science Laboratory rover. *Space Sci. Rev.* 170 (1-4), 583–640.
- 1002 Greeley, R., P.L. Whelley, R.E. Arvidson, N.A. Cabrol, D.J. Foley, B.J. Franklin, P.J. Geissler, M.P.
1003 Golumbeck, R.O. Kuzmin, G.A. Landis, M.T. Lemmon, L.D.V. Neakrase, S.W. Squyres, S. D. Thompson,
1004 2006. Active dust devils in Gusev Crater, Mars: Observations from the Mars Exploration Rover, Spirit. *J.*
1005 *Geophys. Res.* 111, E12S09, doi: 10.1029/2006JE002743.
- 1006 Guzewich, S.D., C.E. Newman, M. de la Torre Juarez, R.J. Wilson, M. Lemmon, M.D. Smith, H.
1007 Kahanpää, A.-M. Harri & the REMS Science Team and MSL Science Team (2016), Atmospheric tides in
1008 Gale Crater, Mars, *Icarus*, 268, 37-49.
- 1009 Guzewich, S., de la Torre-Juárez, M., Newman, C.E., Mason, E., Smith, M.D., Miller, N., Khayat, A.S.J.,
1010 Kahanpää, H., Viúdez-Moreiras, D., Richardson, M. (2021) Gravity Wave Observations by the Mars
1011 Science Laboratory REMS Pressure Sensor and Comparison with Mesoscale Atmospheric Modeling with
1012 MarsWRF. *JGR: Planets*, 126(8), e2021JE006907.
- 1013 Heavens, N. G., D. J. McCleese, M. I. Richardson, D. M. Kass, A. Kleinböhl, and J. T. Schofield (2011),
1014 Structure and dynamics of the Martian lower and middle atmosphere as observed by the Mars Climate
1015 Sounder: 2. Implications of the thermal structure and aerosol distributions for the mean meridional
1016 circulation, *J. Geophys. Res.*, 116, E01010, doi:10.1029/2010JE003713.
- 1017 Heavens, N.G. et al. (2020) A multiannual record of gravity wave activity in Mars’s lower atmosphere from
1018 on-planet observations by the Mars Climate Sounder, *J. Geophys. Res* 341, 113630
- 1019 Hess, S.L., Henry, R.M., Leovy, C.B., Ryan, J.A., Tillman, J.E., (1977). Meteorological results from the
1020 surface of Mars: Viking 1 and 2. *J. Geophys. Res.* 82 (28), 4559–4574.
- 1021 Holstein-Rathlou, C., et al. (2010), Winds at the Phoenix landing site, *J. Geophys. Res.*,
1022 doi:10.1029/2009JE003411
- 1023 Kahanpää, H. & Viúdez-Moreiras, D. (2021). Modelling martian dust devils using in-situ wind, pressure,
1024 and UV radiation measurements by Mars Science Laboratory. *Icarus*, 359, 114207.
1025 <https://doi.org/10.1016/j.icarus.2020.114207>
- 1026 Kass et al. (2016) Interannual similarity in the Martian atmosphere during the dust storm season. *GRL*,
1027 43(12) 6111-6118.
- 1028 Lemmon M.T., M.D. Smith, D. Viudez-Moreiras, M. de la Torre-Juarez, A. Vicente-Retortillo, A.
1029 Munguira, A. Sanchez-Lavega, R. Hueso, G. Martinez, B. Chide, R. Sullivan, D. Toledo, L. Tamppari, T.

- 1030 Bertrand, J.F. Bell III, C. Newman, M. Baker, D. Banfield, J.A. Rodriguez-Manfredi, J.N. Maki, V.
1031 Apestigue (2022), Dust, Sand, and Winds within an Active Martian Storm in Jezero Crater, *Geophys. Res.*
1032 *Lett.* (under review)
- 1033 Mitchell, D.M., Montabone, L., Thomson, S. and Read, P.L. (2015), Polar vortices on Earth and Mars: A
1034 comparative study of the climatology and variability from reanalyses. *Q.J.R. Meteorol. Soc.*, 141: 550-562.
- 1035 Mischna, M. and 14 co-authors (2021), Atmospheric Assessment in Support of Ingenuity Helicopter
1036 Flights, AGU Fall Meeting, New Orleans, LA, December 2021.
- 1037 Montabone, L., Spiga, A., Kass, D. M., Kleinboehl, A., Forget, F., & Millour, E. (2020). Martian year 34
1038 column dust climatology from marsclimate sounder observations: Reconstructed maps and model
1039 simulations. *Journal of Geophysical Research: Planets*, 125, e2019JE006111.
- 1040 Murphy, J.R., Leovy, C.B., Tillman, J.E. (1990) Observations of Martian surface winds at the Viking
1041 lander 1 site. *J. Geophys. Res.* 95(B9), 14555–14576.
- 1042 Newman, C.E., Gómez-Elvira, J., Marín, M., Navarro, S., Torres, J., Richardson, M.I., Battalio, J.M.,
1043 Guzewich, S.D., Sullivan, R., de la Torre-Juárez, M., Vasavada, A.R. & Bridges, N.T. (2017) Winds
1044 measured by the Rover Environmental Monitoring Station (REMS) during the Mars Science Laboratory
1045 (MSL) rover's Bagnold Dunes Campaign and comparison with numerical modeling using MarsWRF.
1046 *Icarus*, 291, 203-231.
- 1047 Newman, C.E., de la Torre, M., Pla-García, J., Wilson, R.J., Lewis, S.R., Neary, L., Kahre, M.A., Forget,
1048 F., Spiga, A., Richardson, M.I., Daerden, F., Bertand, T., Viúdez-Moreiras, D., Sullivan, R., Sánchez-
1049 Lavega, A., Chide, B., Rodriguez-Manfredi, J.A. (2021) Multi-model Meteorological and Aeolian
1050 Predictions for Mars 2020 and the Jezero Crater Region, *Space Science Reviews*, 217(20)
- 1051 Newman, C.E. et. al. (2022) The dynamic atmospheric and aeolian environment of Jezero Crater; Mars,
1052 *Science Advances*, 8(21), eabn3783.
- 1053 Pla-García, J., Rafkin, S.C.R., Kahre, M., Gomez-Elvira, J., Hamilton, V.E., Navarro, S., Torres, J., Marín,
1054 M., Vasavada, A.R., (2016). The meteorology of Gale crater as determined from rover environmental
1055 monitoring station observations and numerical modeling. Part I: Comparison of model simulations with
1056 observations. *Icarus* 280, 103–113. doi:10.1016/j.icarus.2016.03.013.
- 1057 Pla-García, J., Rafkin, S., Martinez, G., de Vicente, A., Newman, C., Savijarvi, H., de la Torre, M.,
1058 Rodriguez-Manfredi, J.A, Gómez, F., Molina, A., Viúdez-Moreiras, D., Ari-Matti, H. (2020)
1059 Meteorological predictions for Mars2020 Perseverance rover landing site at Jezero Crater. *Space Science*
1060 *Reviews*, 216(148)
- 1061 Pla-García, J., et al. (2022) Nocturnal turbulence at Jezero driven by the onset of a low-level jet as
1062 determined from MRAMS numerical modeling and MEDA measurements, *JGR-Planets*, this issue.
- 1063 Rafkin, S. C., J. Pla-Garcia, M. Kahre, J. Gomez-Elvira, V. E. Hamilton, M. Marín, S. Navarro, J. Torres
1064 and A. Vasavada (2016), The meteorology of Gale Crater as determined from Rover Environmental
1065 Monitoring Station observations and numerical modeling. Part II: Interpretation, *Icarus*.
- 1066 Reiss, D., Spiga, A. & Erkeling, G. (2014) The horizontal motion of dust devils on Mars derived from
1067 CRISM and CTX/HiRISE observations. *Icarus*, 227, 8-20.
- 1068 Richardson, M., Wilson, R. (2002) A topographically forced asymmetry in the martian circulation and
1069 climate. *Nature* 416, 298–301.

- 1070 Richardson, M. I., & Newman, C. E. (2018). On the relationship between surface pressure, terrain
1071 elevation, and air temperature. Part I: The large diurnal surface pressure range at Gale Crater, Mars and its
1072 origin due to lateral hydrostatic adjustment. *Planetary and Space Science*, 164, 132–157.
- 1073 Rodríguez-Manfredi et al., (2021) The Mars Environmental Dynamics Analyzer, MEDA. A Suite of
1074 Environmental Sensors for the Mars 2020 Mission Space Science Reviews, 217:48
- 1075 Rodríguez-Manfredi, et. al. (2022) The rich meteorology of Jezero crater over the first 250 sols of
1076 Perseverance on Mars, *Nat. Geoscience*, under review.
- 1077 Ryan, J. A., & Henry, R. M. (1979). Mars atmospheric phenomena during major dust storms, as measured
1078 at surface. *J. Geophys. Res.*, 84(B6), 2821–2829, doi: 10.1029/JB084iB06p02821
- 1079 Sánchez-Lavega, A. et al. (2022) Perseverance studies of the Martian atmosphere over Jezero from pressure
1080 measurements, *JGR-Planets*, this issue.
- 1081 Schieber, J, Minitti, ME, Sullivan, R, et al. Engraved on the rocks—Aeolian abrasion of Martian mudstone
1082 exposures and their relationship to modern wind patterns in Gale Crater, Mars. *Depositional*
1083 *Rec.* 2020; 6: 625– 647.
- 1084 Schon, S, et al. (2012) An overfilled lacustrine system and progradational delta in Jezero crater, Mars:
1085 Implications for Noachian climate, *Planetary and Space Science* 67(1), 28-45
- 1086 Smith, M.D. et al. (2022). Diurnal and Seasonal Variations of Aerosol Optical Depth at Jezero Crater,
1087 Mars. *JGR-Planets*, this issue.
- 1088 Spiga, A., Murdoch, N., Lorenz, R., Forget, F., Newman, C., Rodriguez, S., et al. (2021). A study of
1089 daytime convective vortices and turbulence in the Martian planetary boundary layer based on half-a-year of
1090 InSight atmospheric measurements and large-eddy simulations. *Journal of Geophysical Research:*
1091 *Planets*, 126, e2020JE006511.
- 1092 Stanzel et al. (2008) Dust devil speeds, directions of motion and general characteristics observed by the
1093 Mars Express High Resolution Stereo Camera (2008), 197(1), 39-51.
- 1094 Sullivan, R., Golombek, M., Wilson, G., Greeley, R., Kraft, M., Herkenhoff, K., Murphy, J., Smith, P.
1095 (2000) Results of the Imager for Mars Pathfinder windsock experiment. *J. Geophys. Res.*, 105, 24547–
1096 24562.
- 1097 Sullivan, R., and Kok, J. F. (2017), Aeolian saltation on Mars at low wind speeds, *J. Geophys. Res.*
1098 *Planets*, 122, 2111– 2143, doi:10.1002/2017JE005275.
- 1099 Tyler Jr., D., and J. R. Barnes (2013), Mesoscale modeling of the circulation in the Gale Crater region: an
1100 investigation into the complex forcing of convective boundary layer depths, *International Journal of Mars*
1101 *Science and Exploration* 8, 58-77.
- 1102 Vasavada, A. (2022) Mission Overview and Scientific Contributions from the Mars Science Laboratory
1103 Curiosity Rover After Eight Years of Surface Operations, *Space Sci Rev.* 2022; 218(3): 14.
- 1104 Viúdez-Moreiras, D., Gómez-Elvira, J., Newman, C.E, Navarro, S., Marin, M., Torres, J., de la Torre, M. &
1105 the MSL team. (2019a) Gale Surface Wind Characterization based on the Mars Science Laboratory REMS
1106 Dataset. Part I: Wind Retrieval and Gale’s Wind Speeds and Directions. *Icarus*, 319, 909-925.
- 1107 Viúdez-Moreiras, D., Gómez-Elvira, J., Newman, C.E, Navarro, S., Marin, M., Torres, J., de la Torre, M. &
1108 the MSL team (2019b) Gale Surface Wind Characterization based on the Mars Science Laboratory REMS
1109 Dataset. Part II: Wind Probability Distributions. *Icarus*, 319, 645-656.

- 1110 Viúdez-Moreiras, D., Newman, C.E., de la Torre, M., Martinez, G., Guzewich, S., Lemmon, M., Smith,
 1111 M.D., Pla, J., Harri, A.M., Genzer, M., Vicente, A., Lepinette, A., Rodriguez-Manfredi, J.A., Vasavada,
 1112 and Gómez-Elvira, J., A. (2019c) Effects of the MY34/2018 Global Dust Storm as Measured by MSL
 1113 REMS in Gale Crater. *J. Geophys. Res.: Planets*, 124, 1899–1912. <https://doi.org/10.1029/2019JE005985>.
- 1114 Viúdez-Moreiras, D., Arvidson, R.E., Gómez-Elvira, J., Webster, C., Newman, C.E., Mahaffy, P. &
 1115 Vasavada, A.R. (2020a) Advective fluxes in the Martian regolith as a mechanism driving methane and
 1116 other trace gas emissions to the atmosphere, *Geophysical Research Letters*, 47, e2019GL085694.
- 1117 Viúdez-Moreiras, D., Newman, C.E., Forget, F., Lemmon, M., Banfield, D., Spiga, A., Lepinette, A.,
 1118 Rodriguez-Manfredi, J.A., Gomez-Elvira, J., Pla-Garcia, J., Muller, N., Grott., M. & the TWINS/InSight
 1119 team (2020c). Effects of a large dust storm in the near-surface atmosphere as measured by InSight in
 1120 Elysium Planitia, Mars. Comparison with contemporaneous measurements by Mars Science
 1121 Laboratory. *JGR: Planets*, 125, e2020JE006493. <https://doi.org/10.1029/2020JE006493>
- 1122 Viúdez-Moreiras, D. (2021b) A Three-Dimensional Atmospheric Dispersion Model for Mars. *Progress in*
 1123 *Earth and Planetary Science*, 8(53). <https://doi.org/10.1186/s40645-021-00445-4>.
- 1124 Webster C.R. et al. (2018) Background levels of methane in Mars’ atmosphere show strong seasonal
 1125 variations, *Science*, 360(6393), 1093-1096.
- 1126 Wilson, R. J. & Hamilton, K. P. (1996). Comprehensive model simulation of thermal tides in the Martian
 1127 atmosphere. *Journal of the Atmospheric Sciences*, 53: 1290-1326.
- 1128 Zurek, R.W. (1976). Diurnal tide in the Martian atmosphere. *J. of the Atmospheric Sciences*, 33, 321-337
- 1129 Zurek, R.W & Leovy, C.B. (1981) Thermal tides in the Dusty Martian Atmosphere: A Verification of
 1130 Theory, *Science*, 213, 437-439
- 1131 Zurek, R. W., & Martin, L. J. (1993), Interannual variability of planet-encircling dust storms on Mars, *J.*
 1132 *Geophys. Res.*, 98(E2), 3247–3259
- 1133